iScience

Article

Enhanced dry reforming of methane over nickel catalysts supported on zirconia coated mesoporous silica

Graphical abstract

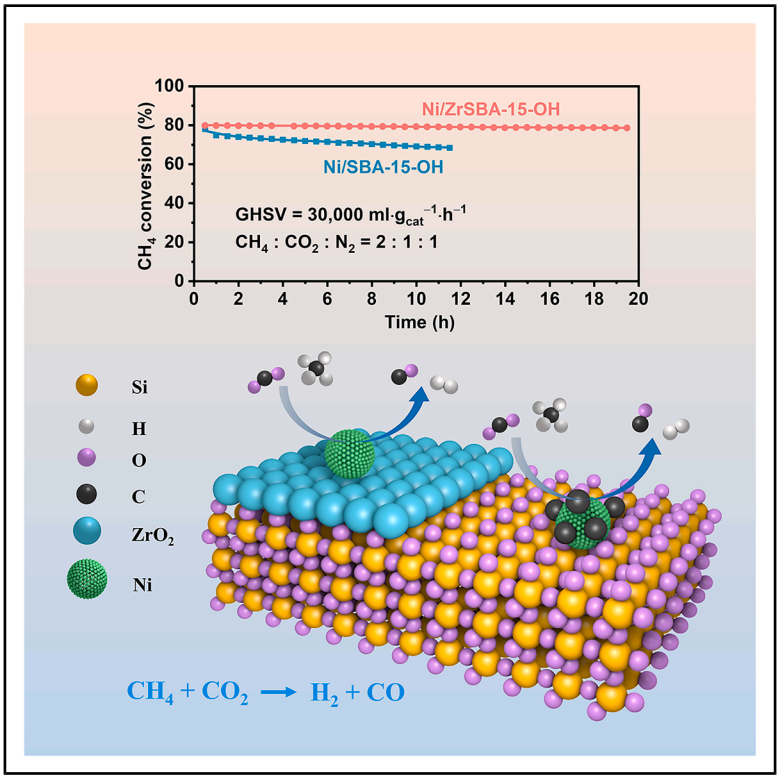

Highlights

- Ni-ZrO_2 interfaces embedded in mesopores enhance coke resistance in DRM
- Ni/ZrSBA-15-OH shows stable DRM performance at 750°C for 20 h with low coking
- Ni-ZrO_2 interaction suppresses methane over-cracking and carbon formation
- Mesoporous structure and oxide interface synergistically improve catalyst stability

Authors

Yi Zhong, Yuhao Peng, Hao Gu, ..., Wei Xiao, Hulei Yu, Dong Gu

Correspondence

huleiyu@scut.edu.cn (H.Y.), dgu@scut.edu.cn (D.G.)

In brief

Chemistry; Materials science; Materials chemistry

Zhong et al., 2025, iScience *28*, 112582
June 20, 2025
https://doi.org/10.1016/j.isci.2025.112582

CellPress

iScience

CellPress
OPEN ACCESS

Article

Enhanced dry reforming of methane over nickel catalysts supported on zirconia coated mesoporous silica

Yi Zhong,[1] Yuhao Peng,[1,4] Hao Gu,[3] Shan Zhang,[5] Feng Ryan Wang,[3] Wei Xiao,[4] Hulei Yu,[2,*] and Dong Gu[1,2,6,*]
[1]The Institute for Advanced Studies, Wuhan University, Wuhan, Hubei 430072, P.R. China
[2]School of Materials Science and Engineering, South China University of Technology, Guangzhou 510640, P.R. China
[3]Department of Chemical Engineering, University College London, London WC1E 7JE, UK
[4]College of Chemistry and Molecular Sciences, Hubei Key Laboratory of Electrochemical Power Sources, Wuhan University, Wuhan 430072, P.R. China
[5]Institute of Materials Science and Devices, Suzhou University of Science and Technology, Suzhou 215011, P.R. China
[6]Lead contact
*Correspondence: huleiyu@scut.edu.cn (H.Y.), dgu@scut.edu.cn (D.G.)
https://doi.org/10.1016/j.isci.2025.112582

SUMMARY

Dry reforming of methane (DRM) offers a sustainable route to convert CH_4 and CO_2 into syngas, addressing both greenhouse gas emissions and energy demand. However, catalyst deactivation due to sintering and coking limits practical applications. In this work, we developed a mesoporous Ni-based catalyst (Ni/ZrSBA-15-OH) featuring abundant Ni-ZrO_2 interfaces and small Ni nanoparticles (5.6 nm) confined within a stable silica framework. This catalyst showed excellent performance, achieving 80% CH_4 and 87% CO_2 conversions at 750°C, with minimal coke formation (0.4 mg g_{cat}^{-1} h^{-1}) and high durability (1.3% CH_4 conversion loss over 20 h). Advanced characterizations (X-ray absorption spectroscopy [XAS], transmission electron microscopy [TEM], H_2-temperature programmed reduction [H_2-TPR], and temperature-programmed surface reaction [TPSR]) revealed that the metal-oxide interface enhances the activation of reactants and stabilizes active sites. Density functional theory (DFT) calculations confirmed that the Ni-ZrO_2 interface increases the energy barrier for CH* dehydrogenation, effectively suppressing carbon deposition. This study provides a rational strategy for designing structurally robust and coke-resistant Ni-based catalysts for efficient DRM.

INTRODUCTION

Dry reforming of methane (DRM) is a promising strategy for converting the major greenhouse gases, carbon dioxide (CO_2) and methane (CH_4), into valuable carbon monoxide (CO) and hydrogen (H_2).[1,2] The resulting syngas serves as a critical feedstock for various chemical processes, including Fischer-Tropsch (F-T) synthesis, methanol production, and even ammonia synthesis.[3–7] The aforementioned catalytic conversion pathway has attracted substantial interest from both academic and industrial communities due to its significant implications, prompting intensified research efforts that have extended to preliminary investigations of commercial viability.[8] Among various DRM catalytic systems, Ahmed S. Al-Fatesh investigated as many as 8 active sites (Fe, Co, Ni, Ru, Rh, Pd, Ir, and Pt), 12 different supports, and 35 promoters. Notably, Ni active sites demonstrate methane and carbon dioxide conversion rates comparable to noble metals, while benefiting from abundant crustal reserves and low cost.[9–12] However, the Ni-based catalysts suffer from nanoparticle (NP) sintering at operating temperatures exceeding the Tammann temperature of metallic Ni (581°C), leading to aggregation and coke formation. Additionally, Ni-based catalysts with active sites in close proximity facilitate successive C–H bond dissociation of CH_4, followed by C–C coupling, which accelerates carbon deposition and shortens the catalyst's operational lifespan.[13] To address these issues, various strategies have been developed, including the incorporation of transition metals (e.g., Mo, W, Bi, Sn, etc.), support modification, and the construction of heterogeneous interfaces with metal oxides or silica.[14–17]

Creating heterogeneous interfaces between metal active sites and various supports has emerged as an effective strategy to enhance catalytic performance and maintain the structural stability of catalysts in photocatalysis, electrocatalysis, as well as thermal catalysis.[18–21] This design concept has also been applied to the development of high-performance DRM catalysts. For example, Dai et al. synthesized Ni nanoparticles (NPs) supported on dendritic mesoporous silica (Ni/DMS) with abundant Ni-silica interfaces, employing a surface spatial confinement strategy.[22] Notably, mesoporous silica provides stable framework structures capable of withstanding harsh reaction conditions. However, the Ni/DMS catalyst faces challenges in preventing the sintering and aggregation of Ni NPs during long-term testing (>700°C) due to relatively weak metal-silica interactions. As a result, many researchers have

explored metal oxides as alternative supports to strengthen metal-support interactions (MSI) and develop more durable catalysts. ZrO_2 is a widely used support material due to its strong anchoring effect on active metal dispersion and its redox capacity, which enables the instantaneous oxidation of carbon deposits. The Ni/ZrO_2 system exhibits finely tuned acid-base properties, particularly in the tetragonal phase, whereas other supports generally display either predominantly acidic or basic sites.[23] Additionally, ZrO_2 can be combined with other elements to form composite supports.[24–26] For example, Ahmed Sadeq Al-Fatesh et al. reported that phosphate-zirconia-supported Ni catalysts exhibited remarkable activity for hydrogen production. This enhanced performance was attributed to multiple CH_4 decomposition sites and sufficient basic surface properties, which facilitate CO_2 activation via both physisorption and chemisorption as carbonate/carboxylate species.[24] While metal oxide supports can stabilize active metal sites to some extent via the strong MSI process, bulk metal oxides still face substantial challenges in preventing the sintering of active metal NPs and structural collapse during catalytic reactions. Therefore, Ni-based catalysts with stable framework structures and robust MSI remain a significant challenge. SiO_2, on the other hand, possesses exceptional catenation properties, second only to carbon, allowing for a diverse range of structural architectures, from nonporous to mesoporous materials. Notably, mesoporous silica offers a high specific surface area that effectively disperses active metal components, while its confinement effect significantly inhibits the sintering of Ni nanoparticles.[27]

Our study aims to combine the advantages of both metal oxide supports and inert carriers by developing a catalyst system that integrates the thermal stability of a silica framework with active sites conducive to DRM reactions. In this study, we utilized silanol-rich mesoporous silica (SBA-15-OH) to enhance the interfacial interaction between silica and zirconia, successfully developing a nickel-based catalyst for dry reforming of methane (Ni/ZrSBA-15-OH). The designed composite catalyst features abundant nickel-zirconia (Ni-ZrO_2) interfaces, integrated with a stable mesoporous silica (SBA-15-OH) framework and strong metal-support interaction (SMSI). Specifically, the Ni/ZrSBA-15-OH catalyst was prepared using a ZrO_2 nanolayer confined within mesoporous silica pore channel (ZrSBA-15-OH) as the support and nickel nitrate as the precursor. The resulting Ni/ZrSBA-15-OH catalyst exhibited abundant Ni-ZrO_2 interfaces, relatively uniform particle sizes (5.6 nm), and a stable framework. Furthermore, this catalyst demonstrated high CH_4 and CO_2 conversion (80% and 87%, respectively) and excellent stability over 20 h at 750°C. Additionally, the Ni/ZrSBA-15-OH catalyst exhibited a significantly lower coke formation rate of 0.4 mg g_{cat}^{-1} h^{-1}, indicating that the creation of metal-oxide heterogeneous interfaces enhances catalytic performance, suppresses coke formation, and efficiently stabilizes the active metal sites. This work presents an effective approach for synthesizing highly stable and durable catalysts.

RESULTS AND DISCUSSION

Microstructures and morphologies of Ni-based catalysts

A composite catalyst with abundant Ni-ZrO_2 interfaces, designated as Ni/ZrSBA-15-OH, was synthesized via consecutive impregnation and calcination. The ZrO_2-coated mesoporous silica support (ZrSBA-15-OH) was prepared through a surface modification using zirconium oxychloride octahydrate ($ZrOCl_2 \cdot 8H_2O$) as a precursor, and a silanol group-rich mesoporous silica (SBA-15-OH) as a support, followed by calcination at 300°C for 4 h in air.[28,29] Nickel nitrate was then deposited onto the ZrSBA-15-OH support and calcined at 500°C for 2 h. Reference samples were synthesized following the same procedure but using different supports, including SBA-15-OH, surface-cast mesoporous ZrO_2 (SCO-Zr), and commercial ZrO_2, yielding catalysts designated as Ni/SBA-15-OH, Ni/SCO-Zr, and Ni/Commercial ZrO_2, respectively.

Low-angle X-ray diffraction (LAXRD) patterns of Ni/SBA-15-OH and Ni/ZrSBA-15-OH catalysts exhibit distinct (100), (110), and (200) diffraction peaks, characteristic of a two-dimensional hexagonal mesoporous structure (Figure 1A). These reflections confirm that both catalysts retain a well-ordered mesostructure similar to the parent SBA-15-OH. The sharpness and intensity of the (100) peak indicate high structural integrity, while the presence of higher-order peaks, such as (110) and (200), further confirms the preservation of long-range mesostructure after metal incorporation. The support materials and reference catalysts were also analyzed (Figure S1). The wide-angle X-ray diffraction (WAXRD) pattern of ZrSBA-15-OH (Figure S1) exhibits a broad array of Bragg diffraction peaks, suggesting that the high-surface-area silica framework promotes the formation of small zirconia crystalline domains (PDF#79–1769).[30] In addition, the WAXRD patterns of Ni/ZrSBA-15-OH and Ni/SBA-15-OH (Figure 1B) display three distinct diffraction peaks at 44.4°, 51.8°, and 76.2°, corresponding to the (101), (012), and (110) crystal planes of cubic nickel oxide (NiO), respectively.[31] The full width at half-maxima (FWHM) of the NiO reflections in Ni/ZrSBA-15-OH is significantly broader than in Ni/SBA-15-OH, indicating smaller NiO particle sizes due to the formation of abundant NiO-ZrO_2 heterogeneous interfaces. It should be noted that, as demonstrated in our previous studies,[28] ZrO_2 forms a tubular structure within the mesoporous silica channels. This unique configuration preferentially promotes NiO-ZrO_2 interfacial formation. Subsequent nitrogen physisorption analyses further corroborate the existence of the ZrO_2 layer. Additional control samples were also characterized, as shown in Figures S1B and S1C. Nitrogen adsorption-desorption isotherms for Ni/ZrSBA-15-OH, Ni/SBA-15-OH, and Ni/SCO-Zr (Figure 1C and S1) exhibit type IV isotherms with distinct H1-type hysteresis loops, indicative of ordered mesoporous structures.[32] The reduction in pore size and weakened peak intensity of Ni/ZrSBA-15-OH clearly demonstrate the uniform coating of a ZrO_2 layer within the mesoporous channels (Figure 1C inset). The nitrogen adsorption capacity of these catalysts and their corresponding supports decreased upon ZrO_2 and/or NiO incorporation compared to the parent SBA-15-OH. Furthermore, the corresponding pore size distribution plots (Figures 1C and S1 inset), obtained using the Barrett-Joyner-Halenda (BJH) algorithm, reveal a significant decrease in maximum pore sizes upon ZrO_2 and/or NiO introduction. This reduction in both nitrogen adsorption capacity and pore size confirms the successful impregnation of ZrO_2 and NiO precursors into the mesoporous silica support. The comprehensive textural parameters of

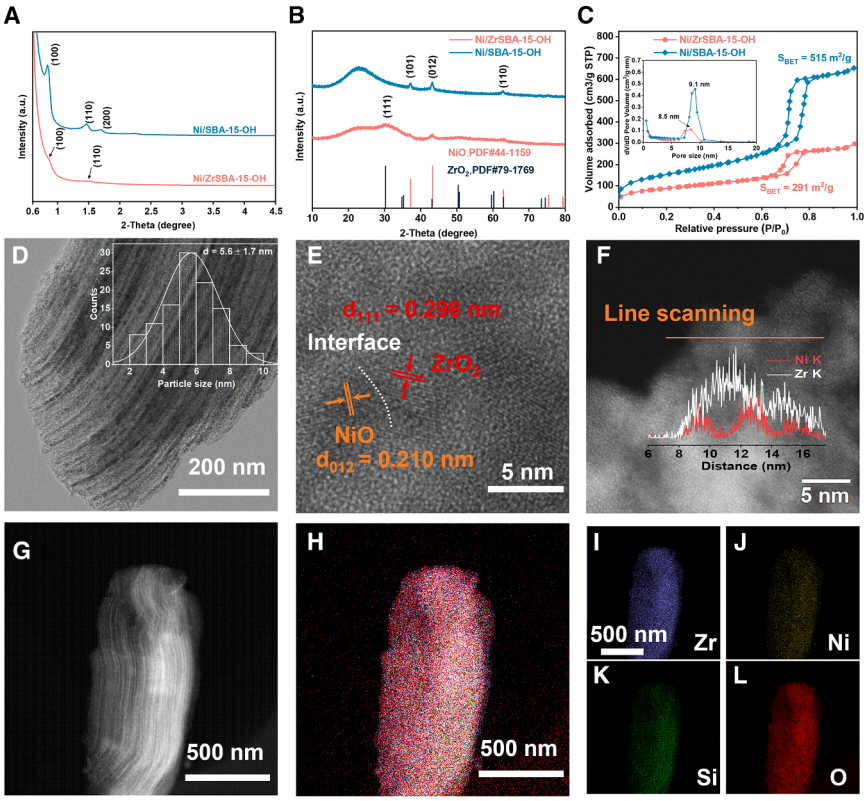

Figure 1. Structural characterization of fresh catalysts

(A–C) (A) LAXRD patterns, (B) WAXRD patterns, (C) nitrogen adsorption-desorption isotherms and corresponding pore size distribution plots (insert) of Ni/SBA-15-OH and Ni/ZrSBA-15-OH catalysts. (D) TEM image of Ni/ZrSBA-15-OH, with NiO particle size distribution shown in the insert.

(E–L) (E) High-resolution TEM image, (F) Aberration-corrected high-angle annular dark-field scanning transmission electron microscopy (AC-HAADF-STEM) image, (G) Scanning transmission electron microscopy (STEM) image, and (H–L) Energy-dispersive X-ray spectroscopy (EDX) elemental mappings of the Ni/ZrSBA-15-OH catalyst. The white dashed line in (f) represents the heterogeneous interfaces between NiO particle and ZrO_2 support.

catalyst carriers and their supported Ni-based catalysts are summarized in Table S1. Additionally, the final Ni content of these catalysts was determined by inductively coupled plasma atomic emission spectrometry (ICP-OES). Specifically, Ni/ZrSBA-15-OH and Ni/SBA-15-OH exhibited Ni loadings of 4.7 wt.% and 5.2 wt.%, respectively.

To investigate the structures and morphologies of the samples, microstructural analysis was conducted using scanning electron microscopy (SEM), transmission electron microscopy (TEM), and STEM. SEM images (Figure S2) of Ni-based catalysts (Ni/ZrSBA-15-OH, Ni/SBA-15-OH, and Ni/SCO-Zr) derived from the SBA-15-OH template reveal rod-like structures similar to the parent SBA-15-OH. Additionally, TEM images (Figures 1D and S3) of Ni/ZrSBA-15-OH and Ni/SBA-15-OH confirm that their structures and morphologies closely resemble their respective supports. Notably, the TEM image of Ni/ZrSBA-15-OH displays a relatively uniform NiO particle size distribution compared to Ni/SBA-15-OH (Figure S3). The average NiO particle sizes of Ni/ZrSBA-15-OH and Ni/SBA-15-OH are 5.6 nm and 11.6 nm, respectively, consistent with WAXRD results. These findings indicate that the ZrO_2-coated support significantly reduces NiO particle size, likely due to surface interactions between NiO and ZrO_2. It should be noted that although the average nanoparticle size of NiO (11.6 nm) exceeds the pore diameter of SBA-15-OH (9.3 nm), this does not preclude the presence of NiO within the mesoporous channels. It is important to note that SBA-15-OH does not consist solely of isolated tubular channels; instead, adjacent channels are interconnected via numerous junctions. These interconnections enable nanoparticles to extend across neighboring pores, facilitating their incorporation.[33] Additionally, nanoparticle growth within the mesopores occurs in a random orientation. In SBA-15-OH, NiO nanoparticles can preferentially grow along the longitudinal axis of the channels, leading to an apparent increase in particle size.

To further confirm the presence of heterogeneous interfaces, high-resolution TEM (HR-TEM) imaging of Ni/ZrSBA-15-OH was performed (Figure 1E). Two distinct interplanar spacings of 0.296 nm and 0.210 nm were identified, corresponding to the (111) plane of ZrO_2 and the (012) plane of NiO, respectively. Additionally, aberration-corrected high-angle annular dark-field STEM (AC-HAADF-STEM) imaging and corresponding elemental line scanning profiles (Figure 1F) reveal overlapping Zr and Ni signals, confirming the formation of a well-defined ZrO_2-NiO interface. In contrast, Ni/SBA-15-OH exhibits only the characteristic (012) plane of NiO, as shown in Figure S3. The microstructures and morphologies of the support and other control samples (e.g., Ni/SCO-Zr, Ni/Commercial ZrO_2) are presented in Figures S4–S6. Furthermore, STEM imaging (Figure 1G) and energy-dispersive X-ray spectroscopy (EDX) mappings (Figures 1H–1L) of Ni/ZrSBA-15-OH, taken perpendicular to the channel direction, reveal a homogeneous distribution of Si, Zr, Ni, and O species. In contrast, STEM imaging and EDX mappings of Ni/SBA-15-OH, which lacks ZrO_2 modification, show significant Ni aggregation on the support surface. This suggests that the absence of metal oxide modification hinders the uniform dispersion of Ni species. Therefore, the ZrO_2 surface modification strategy not only facilitates the formation of NiO-ZrO_2 heterogeneous interfaces but also enhances the stability of catalytically active sites through strong surface interactions.

Catalytic performance of Ni-based catalysts

The catalytic performance of Ni-based catalysts for DRM was evaluated in a fixed-bed reactor at temperature intervals of 50°C within the range of 550°C–800°C, under a weight hourly

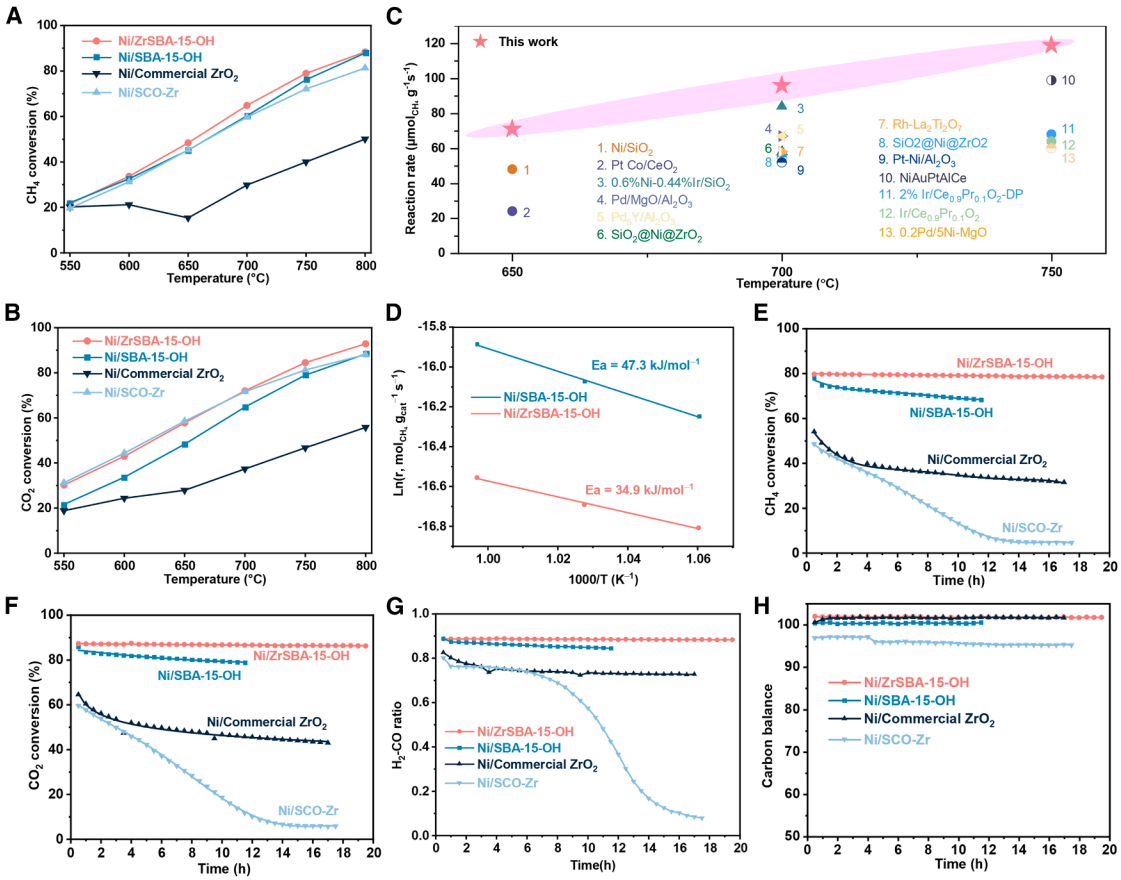

Figure 2. Catalytic performances of Ni-based catalysts in the DRM reaction

(A and B) (A) CH_4 conversion and (B) CO_2 conversion over Ni-based supported catalysts. Reaction conditions: CH_4:CO_2:N_2 = 2:2:1, weight hourly space velocity (WHSV) = 30,000 mL g_{cat}^{-1} h^{-1}.

(C) Comparison of mass-specific activity between Ni/ZrSBA-15-OH and other typical catalysts used in the DRM reaction.

(D) Kinetic studies and calculated activation energy (E_a) for CH_4 over Ni/ZrSBA-15-OH and Ni/SBA-15-OH.

(E and F) (E) CH_4 and (F) CO_2 conversion of Ni-based catalysts as a function of time on stream at 750°C under reaction conditions.

(G and H) (G) H_2/CO ratio and (H) carbon balance over the Ni-based supported catalysts.

space velocity (WHSV) of 30,000 mL g_{cat}^{-1} h^{-1}. Prior to testing, all catalysts were pretreated in an H_2 gas stream at 500°C, followed by exposure to a CH_4:CO_2:N_2 reaction gas mixture (2:2:1). The catalytic activity was recorded using gas chromatography. As shown in Figures 2A and 2B, CH_4 and CO_2 conversions increased significantly with temperature, confirming the strong endothermic nature of the reaction. Notably, the Ni/ZrSBA-15-OH catalyst exhibited superior reactant conversion compared to the control samples (Ni/SBA-15-OH, Ni/SCO-Zr, and Ni/Commercial ZrO_2) across the entire temperature range. At 800°C, CH_4, and CO_2 conversions for Ni/ZrSBA-15-OH reached approximately 88% and 92%, respectively. Microstructural analysis suggests that the enhanced catalytic performance of Ni/ZrSBA-15-OH can be attributed to its Ni-ZrO_2 heterogeneous interfaces, smaller Ni particle size, and stable framework. In contrast, Ni/SBA-15-OH features a stable framework but larger Ni particles, while Ni/SCO-Zr contains Ni-ZrO_2 interfaces but lacks structural stability. It is evident that the Ni/Commercial ZrO_2 catalyst exhibits significantly lower activity compared to other catalysts. This can be attributed to the bulk-phase nature of commercial ZrO_2, which fails to effectively disperse NiO nanoparticles. The larger particle size results in a reduced number of NiO-ZrO_2 interfacial sites, which are crucial for catalytic performance. The synergistic effect of these characteristics in Ni/ZrSBA-15-OH significantly improves catalytic activity. Additionally, CO_2 conversion was consistently higher than CH_4 conversion, likely due to the reverse water-gas shift (RWGS) side reaction.[34,35] The corresponding H_2/CO ratios for Ni-based catalysts are presented in Figure S7, while Figure S8 confirms the inactivity of ZrSBA-15-OH. Compared to reported catalysts (Figure 2C; Table S2), Ni/ZrSBA-15-OH demonstrates superior reactivity. The apparent activation energy (E_a) for CH_4 and CO_2 was determined using the Arrhenius equation (Figures 2D and S9). For CH_4, E_a values for Ni/ZrSBA-15-OH and Ni/SBA-15-OH were 34.9 kJ/mol and 47.3 kJ/mol, respectively, indicating that methane activation is more favorable on Ni/ZrSBA-15-OH. In contrast, E_a for CO_2 was similar for both catalysts (34.7 kJ/mol and 38.7 kJ/mol), suggesting comparable activation capabilities for CO_2.

To assess the long-term stability of Ni-based catalysts, durability tests were conducted at 750°C under atmospheric pressure (Figures 2E and 2F). Notably, the Ni/ZrSBA-15-OH catalyst exhibited excellent stability, with no significant decrease in CH_4 and CO_2 conversion over 20 h of continuous operation. Although Ni/ZrSBA-15-OH and Ni/SBA-15-OH initially showed similar CH_4 and CO_2 conversions, their activities declined by 7% and 10%, respectively, within 11.5 h. This confirms that the introduction of the ZrO_2 interface layer, which forms Ni-ZrO_2 heterogeneous interfaces and stabilizes Ni species, is crucial for enhancing catalyst durability. In contrast, Ni/SCO-Zr and Ni/Commercial ZrO_2, despite also possessing Ni-ZrO_2 heterogeneous interfaces, exhibited significant deactivation over time. Specifically, CH_4 conversion for Ni/Commercial ZrO_2 and Ni/SCO-Zr declined by 23% and 43%, respectively, within 18 h (Figure 2E), while CO_2 conversion followed a similar trend (Figure 2F). This rapid deactivation is likely due to mesostructure collapse of the SCO-Zr support and/or Ni nanoparticle aggregation on different supports. Further analysis of H_2/CO ratios and carbon balance during stability testing at 750°C is presented in Figures 2G and 2H. The Ni/ZrSBA-15-OH catalyst maintained a consistent C/H ratio of ~0.9, making its products suitable as high-quality feedstock for further chemical processes. In contrast, other catalysts suffered from either excessive C/H ratio fluctuations or instability. The carbon balance, estimated by comparing the carbon content in reactants and products, approached 1 for Ni/ZrSBA-15-OH, Ni/SBA-15-OH, and Ni/Commercial ZrO_2, while the Ni/SCO-Zr catalyst showed lower carbon utilization efficiency (Figure 2H). Overall, the Ni/ZrSBA-15-OH catalyst, with its abundant Ni-ZrO_2 heterogeneous interfaces, small Ni particle size, and stable framework, demonstrated the highest catalytic activity and stability. These findings highlight that constructing stable metal-ZrO_2 interfaces and utilizing thermally stable silica supports are effective strategies for achieving efficient DRM reactions.

Electronic structures of Ni-based catalysts

X-ray absorption spectroscopy (XAS) was employed to investigate the chemical valence and coordination structures of Ni species. The X-ray absorption near-edge structure (XANES) spectrum reveals that the K-edge position of Ni in Ni/ZrSBA-15-OH lies between that of Ni foil and NiO, suggesting a transitional oxidation state between 0 and +2 (Figure 3A). This suggests electron transfer between Ni and ZrO_2.[36,37] The peak at 8334 eV corresponds to quadrupole transitions of *1s* photoelectrons to Ni*3d*-O*2p* hybridized orbitals in the oxide phase, the metallic phase, or a combination of both. The peak at 8352 eV is attributed to transitions of *1s* electrons to Ni*4p*-O*2p* orbitals in the oxide phase.[36,38] The intensity of these peaks in Ni/ZrSBA-15-OH falls between those of Ni foil and NiO, with a closer resemblance to the oxide spectrum. Moreover, the spectral features in the 8335–8340 eV region differ from those of Ni foil and NiO, indicating a distinct local chemical environment for Ni. Extended X-ray absorption fine structure (EXAFS) fitting further clarifies the coordination environment of Ni/ZrSBA-15-OH. The R-space comparison (Figure 3B) and fitting results (Figure S10; Table S3) reveal predominant first-shell Ni-O and Ni-Ni/Zr coordination, along with second-shell Ni-O-Ni/Zr coordination. Detailed fitting parameters are provided in the corresponding table. The k-space analysis confirms strong agreement between experimental data and simulations (Figure 3C). Additionally, wavelet transform (WT) analysis (Figures 3D–3F) supports these findings, identifying dominant first-shell Ni-O and Ni-Ni/Zr coordination, as well as second-shell Ni-O-Ni/Zr coordination, consistent with the R-space fitting results.[39,40] In summary, XAS analysis confirms that Ni/ZrSBA-15-OH exhibits a distinct chemical environment for Ni, arising from strong interactions between Ni and ZrO_2 at the interface.

X-ray photoelectron spectroscopy (XPS) was conducted to analyze the valence states of the pre-catalysts and reduced catalysts. XPS of Ni $2p_{3/2}$ on the fresh Ni/ZrSBA-15-OH and Ni/SBA-15-OH catalysts (Figures S11A and S11D, respectively) showed the Ni^{2+} signal at around 857.0 eV. Specifically, the Ni $2p_{3/2}$ main peaks of the Ni/ZrSBA-15-OH and Ni/SBA-15-OH catalysts are located at 856.8 eV and 857.0 eV, respectively, while the shoulder peaks on the right side (both at 854.2 eV) correspond to the spin-orbit splitting of the main peaks.[37,41–43] The binding energy data indicate that the valence state of Ni in both the Ni/ZrSBA-15-OH and Ni/SBA-15-OH catalysts is +2. The peaks located near 862 eV are a satellite peak. However, the 0.2 eV difference in the binding energy positions of the Ni $2p_{3/2}$ main peaks between the two catalysts suggests that the electron density of Ni may differ in these two systems. The O *1s* spectra were deconvoluted into two peaks (Figures S11B and S11E). The peaks located at 532.6 eV (Ni/ZrSBA-15-OH) and 533.1 eV (Ni/SBA-15-OH) can be assigned to the lattice oxygen of SiO_2, while those at 530.1 eV (Ni/ZrSBA-15-OH) and 529.6 eV (Ni/SBA-15-OH) correspond to the lattice oxygen of metal oxides.[44–46] It is observed that the Ni/ZrSBA-15-OH catalyst exhibits a higher content of metal oxide lattice oxygen. The Zr *3d* peaks exhibit well-defined symmetry, allowing them to be fitted as a single doublet (Figures S11C and S11F). For the Ni/ZrSBA-15-OH catalyst, the Zr $3d_{5/2}$ and $3d_{3/2}$ peaks are located at 182.9 eV and 185.2 eV, respectively, while for the Ni/SBA-15-OH catalyst, they appear at 183.0 eV and 185.3 eV.[47–49] The minimal binding energy shifts ($\leq$0.3 eV) suggest that the electron density of the Zr/SBA-15-OH support remains largely unchanged before and after Ni loading. The O *1s* peaks of the ZrSBA-15-OH support (Figure S12A) were deconvoluted similarly to previous results, with the peak at 533.0 eV assigned to lattice oxygen in SiO_2 and the peak at 530.6 eV attributed to lattice oxygen in metal oxides (ZrO_2)

The reduced catalyst was also characterized by XPS. Shown as Figure 3G, the peaks located at 853.5 eV (Ni/ZrSBA-15-OH) and 853.1 eV (Ni/SBA-15-OH) are attributed to the $2p_{3/2}$ orbital of metal nickel (Ni^0), while the peaks at 856.9 eV (Ni/ZrSBA-15-OH) and 856.8 eV (Ni/SBA-15-OH) correspond to the $2p_{3/2}$ orbital of divalent nickel (Ni^{2+}). The peaks in the range of 862.0–863.0 eV are assigned to satellite peaks. The results indicate the co-existence of divalent nickel (Ni^{2+}) and zerovalent nickel (Ni^0), with metallic Ni comprising 45% in the Ni/SBA-15-OH catalyst and 38% in the Ni/ZrSBA-15-OH catalyst, indicating greater reduction resistance in the Ni/ZrSBA-15-OH catalyst. Divalent nickel may be attributed to the exposure of the reduced sample to air during XPS testing. Meanwhile, by comparing the binding energy positions, it is observed that the $2p_{3/2}$ peaks of

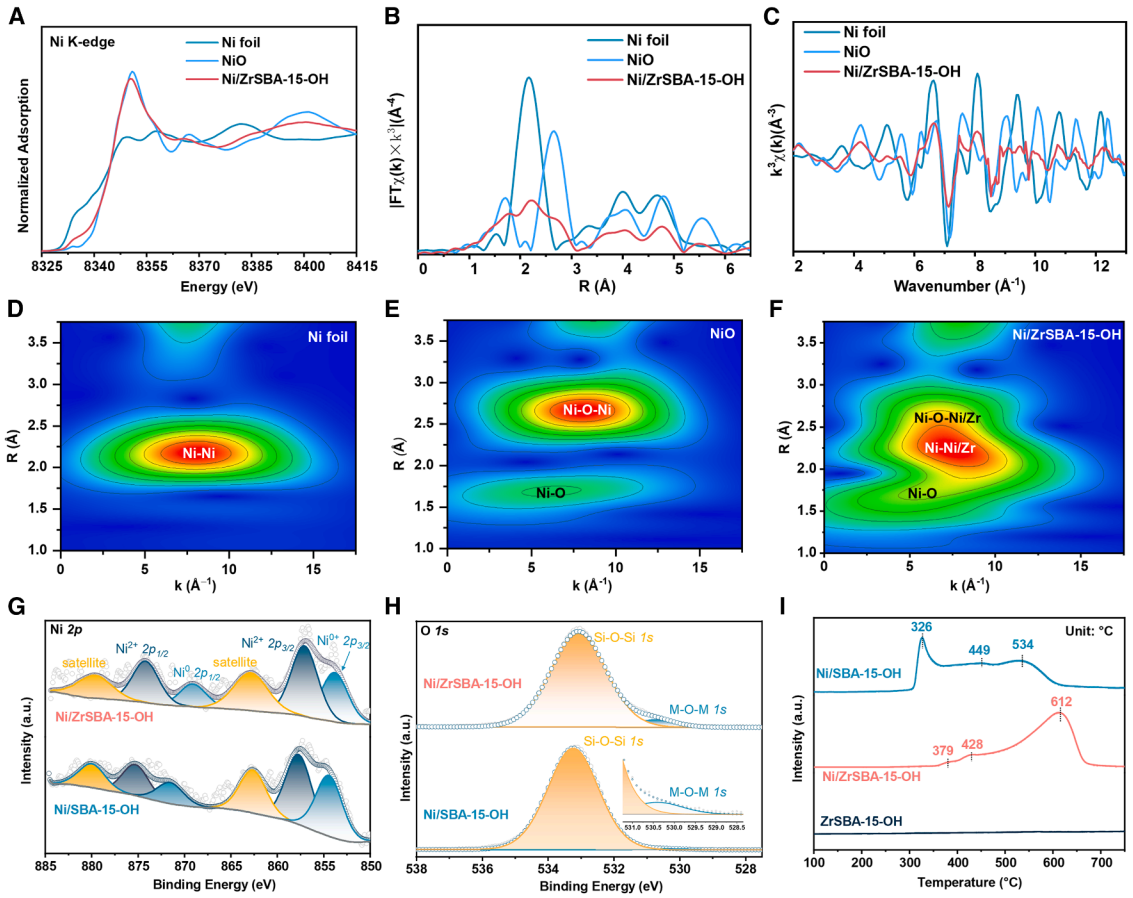

Figure 3. Characterization of Ni-ZrO_2 Interactions

(A) Normalized Ni K-edge XANES spectra of Ni/ZrSBA-15-OH, Ni foil, and NiO.

(B) Fourier transform (FT)-EXAFS spectra of Ni/ZrSBA-15-OH compared with Ni foil and NiO.

(C–H) (C) k^3-weighted Fourier transformed EXAFS spectra of Ni foil, NiO, and Ni/ZrSBA-15-OH. Wavelet transform (WT) results of the EXAFS signals for (D) Ni foil, (E) NiO, and (F) Ni/ZrSBA-15-OH. XPS analysis of (G and H) Ni/ZrSBA-15-OH and Ni/SBA-15-OH after H_2 reduction for 2 h at 500°C.

(I) H_2-TPR profiles of Ni/ZrSBA-15-OH and Ni/SBA-15-OH under a heating rate of 10 °C min^{-1} and an H_2 flow rate of 50 mL min^{-1}.

metal nickel in the two catalysts differ by 0.4 eV, indicating a variation in electron density. In contrast, the $2p_{3/2}$ peaks of divalent nickel (Ni^{2+}) show no significant difference. Similarly, the O *1s* peaks located at 530.4 eV (Ni/ZrSBA-15-OH and Ni/SBA-15-OH) are assigned to lattice oxygen in metal oxides (Figure 3H), while the peaks at 532.9 eV (Ni/ZrSBA-15-OH) and 533.1 eV (Ni/SBA-15-OH) correspond to lattice oxygen in silica. That means, for the oxygen in metal-oxygen bonds (M–O), there is no significant difference in binding energy for Ni/ZrSBA-15-OH and Ni/SBA-15-OH. And the *O 1s* spectrum shows a higher metal-oxygen content in the Ni/ZrSBA-15-OH catalyst (6.51%) compared to the Ni/SBA-15-OH catalyst (2.28%). The Zr *3d* peaks of the ZrSBA-15-OH support and Ni/ZrSBA-15-OH catalyst are located at 183.2 eV and 182.8 eV (Figures S12B and S12C), respectively, indicating an increase in electron density around Zr after Ni loading. The comparative analysis of XPS binding energies reveals that while the O *1s* binding energy remains essentially unchanged after reduction, the metal Ni $2p_{3/2}$ binding energy exhibits an increase, and the Zr *3d* binding energy decreases upon Ni loading. These observations collectively hypothesize that electrons are transferred from Ni species to the ZrO_2 region, suggesting a potential interaction between Ni species and ZrO_2.[43,50]

To further validate the strong interaction between Ni and ZrO_2, H_2-temperature programmed reduction (H_2-TPR) was performed on the pre-catalysts (Figures 3I and S13). The support material (ZrSBA-15-OH) exhibited no reduction peaks, indicating that ZrO_2 remains stable and does not undergo reduction up to 750°C. Three distinct reduction peaks were observed in the Ni-based catalysts, corresponding to different reduction steps.[51] The first peak is attributed to the reduction of free NiO nanoparticles. The second peak corresponds to the reduction of NiO weakly interacting with the support, while the third peak at higher temperatures represents the reduction of NiO nanoparticles with strong metal-support interactions.[52–54] During H_2-TPR, Ni/ZrSBA-15-OH exhibited a dominant H_2 consumption in the third reduction stage, with a reduction temperature of 78°C higher than that of Ni/SBA-15-OH. This significant increase in reduction temperature further confirms the strong interaction between ZrO_2 and Ni. A comparison of the reduction peak positions

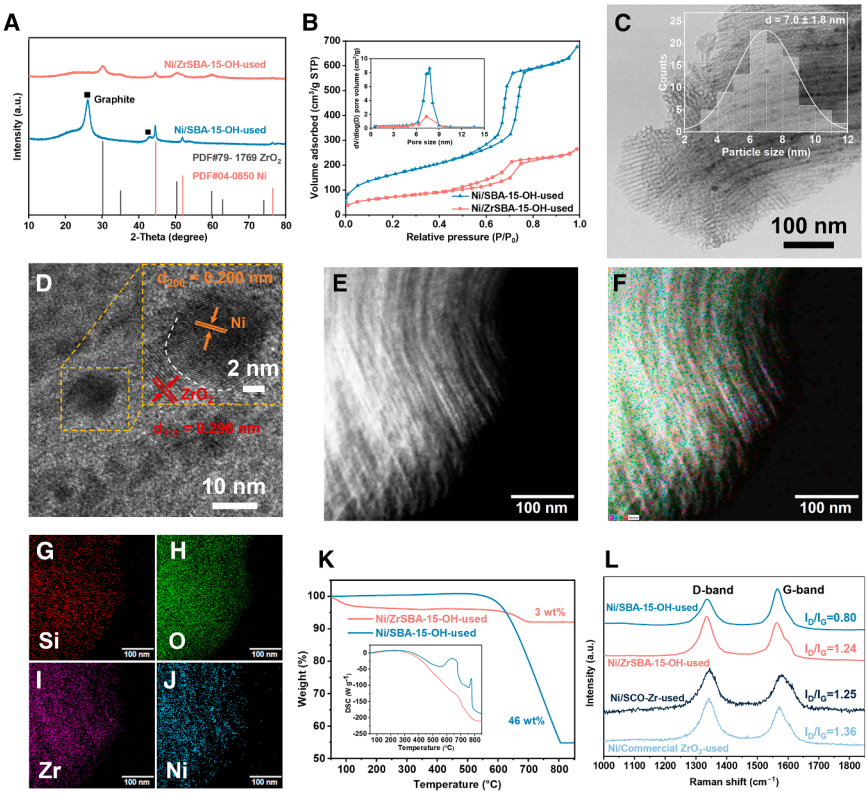

Figure 4. Structural characterization of spent catalysts

(A and B) (A) WAXRD patterns, (B) nitrogen adsorption-desorption isotherms and corresponding pore size distribution plots (insert) of Ni/SBA-15-OH-used and Ni/ZrSBA-15-OH-used catalysts.

(C and D) (C) TEM image and (D) HR-TEM images of Ni/SBA-15-OH-used.

(E–J) (E) STEM image and (F–J) corresponding EDX mappings of Ni/ZrSBA-15-OH-used.

(K and L) (K) TGA curves with corresponding DSC profiles (insert) and (L) Raman spectra of Ni/SBA-15-OH-used, Ni/ZrSBA-15-OH-used, Ni/SCO-Zr and Ni/Commercial ZrO_2 catalysts.

between Ni/Commercial ZrO_2 and Ni/SCO-Zr catalysts reveals distinct hydrogen consumption behaviors. For the Ni/SCO-Zr catalyst, hydrogen consumption is predominantly concentrated in the reduction peak region at 485°C, whereas the Ni/Commercial ZrO_2 catalyst exhibits hydrogen consumption near 328°C. These results suggest that the reduction of NiO is not solely governed by Ni-ZrO_2 interactions but is also influenced by the mesoporous structure. The confinement effect of the mesoporous framework may hinder the reduction of NiO.

Structural characterization of spent catalysts

To evaluate the structural stability of Ni-based catalysts, the spent Ni/ZrSBA-15-OH and Ni/SBA-15-OH samples were analyzed after the stability test. XRD patterns (Figure 4A) of the spent Ni/SBA-15-OH catalyst exhibited distinct diffraction peaks corresponding to graphite, whereas no such peaks were observed for the spent Ni/ZrSBA-15-OH catalyst. This result indicates that the Ni/ZrSBA-15-OH catalyst experiences negligible carbon deposition compared to Ni/SBA-15-OH. The broad FWHM of the ZrO_2 diffraction peaks in the spent Ni/ZrSBA-15-OH catalyst remained largely unchanged compared to the fresh catalyst, suggesting that the mesoporous support, with its high surface area and functional groups, effectively stabilizes the ZrO_2 layer within the mesoporous channels. Additionally, characteristic diffraction peaks corresponding to metallic Ni species were observed in both spent catalysts. However, the FWHM of these peaks in the Ni/SBA-15-OH sample was significantly narrower than that in the Ni/ZrSBA-15-OH sample, indicating that the ZrO_2 layer effectively prevents Ni particle sintering and enhances stability. Figure 4B presents the nitrogen adsorption-desorption isotherms and pore size distribution plots of the spent catalysts. A substantial decrease in specific surface area, pore volume, and peak pore size was observed due to carbon deposition and pore blockage (Table S4). The significant reduction in the specific surface area of Ni/SCO-Zr suggests that its mesoporous structure was severely degraded after the reaction (Figures S14A and S14B; Table S4). To restore the catalysts, the spent samples were treated in air at 800°C to remove surface coke. After treatment, their textural parameters largely returned to levels comparable to those of the fresh catalysts. Notably, the Ni/SCO-Zr catalyst exhibited near-complete restoration of its structural properties (Figures S14C and S14D; Table S5). These findings confirm that both Ni/ZrSBA-15-OH and Ni/SBA-15-OH catalysts, utilizing SBA-15-OH as a rigid framework, demonstrate high structural stability during the DRM reaction.

The microstructures and morphologies of the spent catalysts were further analyzed using SEM and TEM techniques. SEM images of the four catalysts (Figure S15) reveal that the Ni/ZrSBA-15-OH catalyst maintains a clean surface, indicating negligible carbon deposition. In contrast, minor carbon accumulation observed on the Ni/SCO-Zr catalyst is likely due to its rapid deactivation during the reaction. TEM images further support this conclusion. The Ni/ZrSBA-15-OH-used catalyst (Figure 4C) shows no obvious coke formation and exhibits relatively smaller Ni particles (7.0 nm, Figure 4C, inset) compared to the Ni/SBA-15-OH-used catalyst (24.0 nm, Figure S16A inset). In contrast, numerous carbon whiskers, such as carbon nanotubes (Figure S16A), are clearly visible on the surface of the Ni/SBA-15-OH-used catalyst, confirming severe carbon deposition. This behavior is likely attributed to the larger Ni particle size formed during the stability test (11.6–24.0 nm), a hypothesis confirmed by TEM images and particle size distribution analysis. The HR-TEM image (Figure 4D) of Ni/ZrSBA-15-OH-used reveals a well-defined interface between ZrO_2 (111) and Ni (200), demonstrating that the metal-ZrO_2 interface remains intact even after 20 h of stability testing. STEM and EDX spectroscopy

(Figures 4E–4J) further confirm a uniform elemental distribution, with only slight nickel aggregation. Notably, no significant carbon whisker formation was observed around the ZrO_2-Ni interface, consistent with the catalyst's enhanced durability. For Ni/SBA-15-OH-used catalyst, TEM images (Figure S16B) show that metallic Ni nanoparticles are encapsulated by multilayer graphite with a lattice spacing of 0.340 nm, further evidencing severe carbon deposition. Significant carbon deposition is clearly observable for the Ni/SCO-Zr catalyst, with distinct lattice fringes of carbon nanotubes also visible (Figures S16C and S16D), and particle size statistics reveal an average diameter of 21.2 nm (Figure S16C inset). Notably, the variation in particle size of Ni/SCO-Zr before and after the reaction follows a similar trend with Ni/SBA-15-OH. TEM images of Ni/Commercial ZrO_2 demonstrate a pronounced growth in Ni nanoparticle size, reaching an average diameter of 41.8 nm. Furthermore, a substantial number of Ni nanoparticles detach from the support and become dispersed freely after the reaction (Figures S16E and S16F). This observation indicates the instability of active sites in the Ni/Commercial ZrO_2 catalyst, which likely contributes to its rapid deactivation.

To quantify the coke content in the spent catalysts, thermogravimetric analysis (TGA) was conducted. As shown in Figure 4K, Ni/ZrSBA-15-OH-used and Ni/SBA-15-OH-used exhibit distinct weight losses of 3.0 and 46 wt. %, respectively, after stability tests of approximately 20 and 10.5 h.[22,55,56] This corresponds to carbon accumulation rates of 0.4 and 26 mg g_{cat}^{-1} h^{-1}, respectively, confirming the superior coke resistance of the Ni/ZrSBA-15-OH catalyst. To further analyze the nature of carbon deposition, Raman spectroscopy was performed (Figure 4L). During DRM, two types of carbon deposits typically form[57,58]: (1) low-crystallinity, disordered carbon that can be readily removed in an oxidizing atmosphere and (2) highly graphitized carbon, which is more stable and difficult to eliminate, leading to catalyst deactivation. The Raman spectra of the spent catalysts reveal two distinct peaks at 1,343 cm^{-1} and 1,588 cm^{-1}, corresponding to the D-band and G-band of carbon, respectively.[59–63] The D-band (1,343 cm^{-1}) represents disordered, defect-rich carbon that can be more easily removed, while the G-band (1,588 cm^{-1}) reflects highly ordered graphitized sp^2 carbon, which strongly adheres to the catalyst surface and blocks active sites, impairing catalytic performance. The relative intensity ratio of the D-band to G-band (I_D/I_G) serves as a key parameter for assessing the structural defects of carbon deposits and indirectly reflects catalyst stability, yielding values of 0.80 for Ni/SBA-15-OH-used, 1.24 for Ni/ZrSBA-15-OH-used, 1.25 for Ni/SCO-Zr, and 1.36 for Ni/Commercial ZrO_2 catalysts. Notably, all ZrO_2-containing catalysts exhibited I_D/I_G ratios exceeding 1 after stability testing, indicating that ZrO_2 promotes the formation of highly disordered carbon species, which is easier to remove. Under conditions of comparable mesostructural stability, the elevated I_D/I_G ratio may constitute an additional factor contributing to the superior catalytic durability of Ni/ZrSBA-15-OH relative to Ni/SBA-15-OH.

Reaction mechanism for the DRM reaction

To elucidate the reaction pathways of the DRM, highly sensitive temperature-programmed surface reaction (TPSR) experiments, including CH_4-TPSR and CO_2-TPSR, were conducted.[64–66] Freshly prepared catalysts (NiO/ZrSBA-15-OH and NiO/SBA-15-OH) were first pretreated with a 5 vol % H_2/Ar gas mixture before introducing a 20 vol % CH_4/Ar gas mixture into the reactor while simultaneously recording the corresponding mass signals. As shown in Figures 5A and 5C, the initial CH_4 decomposition temperatures for Ni/ZrSBA-15-OH and Ni/SBA-15-OH were approximately 320°C and 200°C, respectively. This indicates that the strong metal-support interactions in Ni/ZrSBA-15-OH slightly reduce CH_4 activation. The dissociation of CH_4 intensified as the reaction temperature increased, with a significantly stronger H_2 signal at ~620°C for Ni/SBA-15-OH compared to 570°C for Ni/ZrSBA-15-OH. Notably, the temperature corresponding to the highest CH_4 dissociation rate was lower for Ni/ZrSBA-15-OH, suggesting its superior low-temperature catalytic activity. Additionally, CO signals were detected in both samples, originating from the reaction of C* or CH_x* intermediates with surface oxygen species (e.g., hydroxyl groups).[67] To further investigate the conversion pathways of C* or CH_x* intermediates, a 20 vol % CO_2/Ar gas mixture was introduced into the reactor. As shown in Figures 5B and 5D, the coke gasification temperatures for Ni/ZrSBA-15-OH and Ni/SBA-15-OH were approximately 650°C and 700°C, respectively. The relatively weak CO signal in the CH_4-treated Ni/ZrSBA-15-OH sample indicates lower carbon deposition on its surface, leading to enhanced durability under stability tests. This observation aligns with the catalyst's stability performance. Based on the TPSR-MS analysis, the Ni/ZrSBA-15-OH catalyst, with its abundant Ni-ZrO_2 heterogeneous interfaces, small particle size, and stable framework, exhibited a lower CH_4 dissociation temperature and coke gasification temperature than Ni/SBA-15-OH. These structural features of Ni/ZrSBA-15-OH catalyst provide a well-balanced mechanism for reactant activation and coke removal, resulting in improved catalytic stability.[61]

In-situ diffuse reflectance infrared Fourier transform spectroscopy (DRIFTS) was employed to investigate the behavior of methane molecules during the reaction process. After *in-situ* reduction of the catalysts at 500°C, a 20% concentration of methane was introduced, and the corresponding spectra were recorded (Figures 5E and 5F). Over time, both catalysts exhibited a characteristic methane signal at 3,016 cm^{-1}. However, notable differences were observed between the two catalysts. For the Ni/SBA-15-OH catalyst, distinct CO_2 peaks (2,362 cm^{-1}) and CO peaks (2,175 cm^{-1} and 2,076 cm^{-1}) appeared within 2 min, suggesting that active oxygen on the catalyst surface facilitated the oxidation of deposited carbon. In contrast, for the Ni/ZrSBA-15-OH catalyst, weak CO_2 peaks were observed only after 7 min. The delayed appearance and lower intensity of these peaks indicate that carbon deposition on the Ni/ZrSBA-15-OH catalyst is more challenging, further demonstrating its reduced methane decomposition ability. The evolution of hydroxyl groups followed a similar trend for both catalysts, suggesting analogous reaction pathways (Figure S17). Overall, the *in-situ* DRIFTS results confirm that the Ni-Zr interface suppresses excessive methane dissociation and mitigates carbon deposition.

DFT calculations

To further understand the mechanism behind the carbon resistance of Ni/ZrSBA-15-OH, Figure 6 illustrates the energy profiles

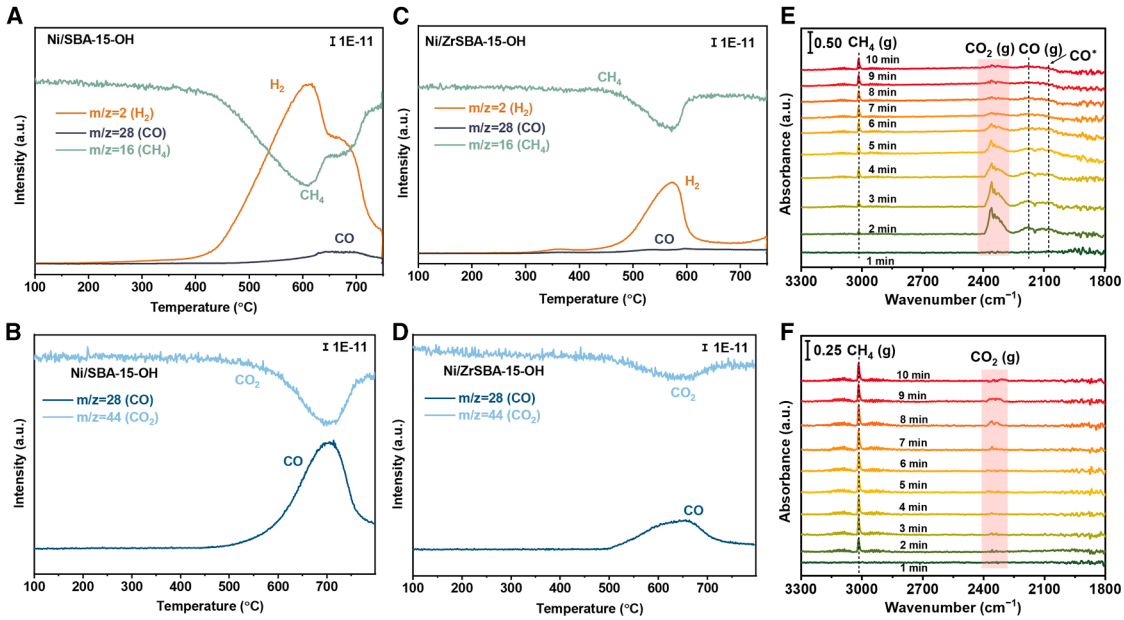

Figure 5. TPSR-MS and *in-situ* DRIFTS analysis of DRM mechanisms

TPSR-MS profiles of Ni/SBA-15-OH (A) and Ni/ZrSBA-15-OH (C) after CH_4 introduction. TPSR-MS signals of Ni/SBA-15-OH (B) and Ni/ZrSBA-15-OH (D) after CO_2 introduction following CH_4 treatment. *In-situ* diffuse reflectance infrared Fourier transform spectroscopy (DRIFTS) of Ni/SBA-15-OH (E) and Ni/ZrSBA-15-OH (F) under a CH_4 atmosphere.

for methane cracking pathway on Ni-ZrO_2 interface and Ni-SiO_2 interface. Obviously, the step, $CH_2^* \rightarrow CH^* + H^*$ and $CH^* \rightarrow C^* + H^*$serves as the rate-determining step for Ni/SBA-15-OH and Ni/ZrSBA-15-OH, respectively. Based on the energy barrier analysis, the initial dissociation step of methane ($CH_4^* \rightarrow CH_3^* + H^*$) exhibits a significantly lower activation barrier on Ni/ZrSBA-15-OH (1.89 eV) compared to Ni/SBA-15-OH (2.06 eV), indicating enhanced activity in the Ni/ZrSBA-15-OH. The subsequent two reaction steps demonstrate nearly identical energy barrier values for the two catalysts, with only 0.1 eV difference observed in both steps. The calculations reveal that the complete decomposition of methane into C* is significantly more challenging on Ni/ZrSBA-15-OH, with an energy barrier of 2.72 eV, compared to only 1.95 eV on Ni/SBA-15-OH. This aligns

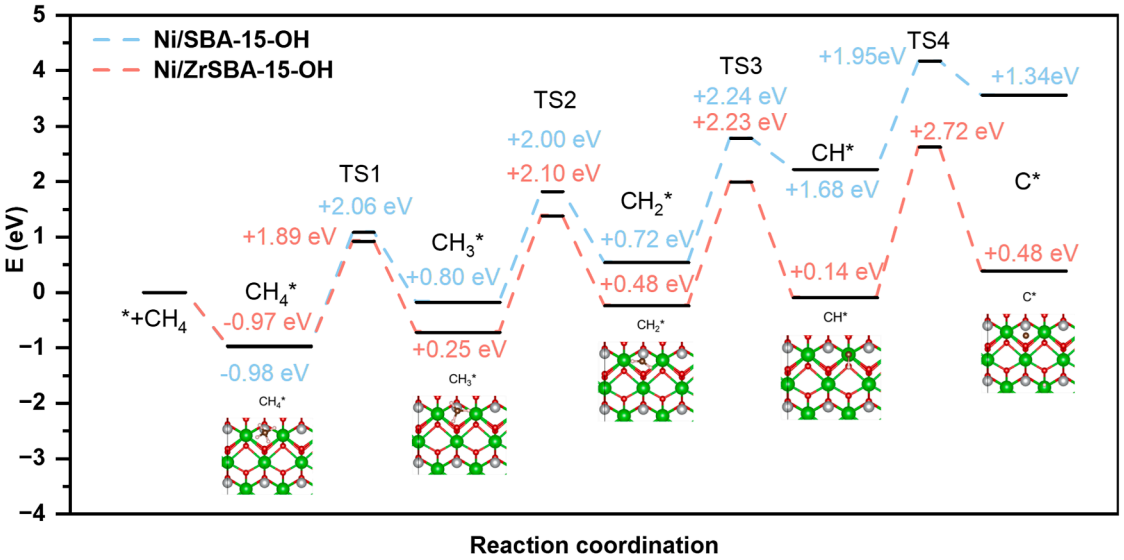

Figure 6. Reaction energy profiles for CH_4 activation on different interfaces

Energy diagrams for $CH_4^* \rightarrow CH_3^* + H^*$, $CH_3^* \rightarrow CH_2^* + H^*$, $CH_2^* \rightarrow CH^* + H^*$ and $CH^* \rightarrow C^* + H^*$ on Ni/ZrSBA-15-OH (Ni-ZrO_2 interface) and Ni/SBA-15-OH (Ni-SiO_2 interface).

with the experimental findings from TPSR and *in-situ* DRIFTS analysis. The results suggest that at the Ni-ZrO_2 interface, the final step of methane dehydrogenation—the removal of the last hydrogen atom to form carbon—is energetically unfavorable, effectively suppressing carbon deposition. Although the Ni/ZrSBA-15-OH catalyst exhibits a lower reaction energy for the final step (CH* → C* + H*) compared to the Ni/SBA-15-OH catalyst, we contend that this reaction step remains more unfavorable on the Ni/ZrSBA-15-OH catalyst. Under the high-temperature environment of 750°C, thermodynamic constraints exert a diminished influence, while kinetic factors dominate the reaction dynamics. Specifically, the Ni/ZrSBA-15-OH catalyst demonstrates a higher energy barrier and consequently a slower reaction rate for this step. The higher energy barrier in the final step may be attributed to differences in CH* adsorption sites. At the Ni-ZrO_2 interface, CH* adsorption occurs at the side position of Ni atoms, whereas on the Ni-SiO_2 interface, adsorption takes place at the top position of Ni atoms. This structural difference likely contributes to the superior coke resistance of Ni/ZrSBA-15-OH. Some recently DFT works for Ni-ZrO_2 system also have studied the effect of interface.[68–72] ZrO_2 effectively reduces the activation energy of reactant molecules through heterointerface formation with metals, while its abundant oxygen vacancies facilitate the adsorption of CO_2 and other reactants. For instance, Wang et al.[73] elucidated the role of Ni-ZrO_2 interfaces in adsorption and activation processes. Their work demonstrated that CO_2 adsorption is more stable on Ni sites (adsorption energy: −0.84 eV), whereas O and OH species preferentially adsorb at Ni-ZrO_2 interfaces. This behavior stems from the high d-band energy of ZrO_2 and SMSI. Notably, interfacial sites significantly lower the activation barrier for CO_2 dissociation, while Ni sites exhibit superior CH_4 activation.

Conclusion

In summary, we developed a Ni/ZrSBA-15-OH catalyst featuring abundant Ni-ZrO_2 interfaces, uniform particle sizes (5.6 nm), and a robust framework structure using a surface-modification approach followed by impregnation-calcination. This catalyst demonstrated high CH_4 and CO_2 conversions of 80% and 87%, respectively, along with excellent stability for approximately 20 h at 750°C. Additionally, the Ni/ZrSBA-15-OH catalyst exhibited a significantly lower coke formation rate of 0.4 mg g_{cat}^{-1} h^{-1}. Comprehensive structural characterization and reaction behavior analysis confirmed that the formation of metal-oxide heterogeneous interfaces in Ni/ZrSBA-15-OH effectively enhances catalytic performance, suppresses coke formation, and stabilizes the active metal sites. Furthermore, a dynamic balance between coke formation and elimination was observed on the catalyst surface. DFT calculations further revealed that the Ni/ZrSBA-15-OH catalyst exhibits a higher energy barrier for CH* dehydrogenation to C*, thereby improving resistance to carbon deposition. This approach offers a promising strategy for designing highly stable Ni-based composite catalysts for the DRM reaction including in thermal catalysis and photocatalysis.

Limitations of the study

Building upon this research, we plan to increase the WHSV to evaluate the stability and anti-coking performance of Ni/ZrSBA15-OH under higher flow conditions. Additionally, we outline future research directions, including further investigations into defect modulation and *in-situ* studies of reaction mechanisms. The Ni/ZrSBA-15-OH catalyst with Ni-ZrO_2 interfaces may also exhibit potential in other fields (e.g., photocatalysis and electrocatalysis), so we have listed some relevant literature. (Table S8). As for the novelty, we developed highly stable mesoporous catalysts for DRM, featuring a unique Ni-ZrO_2 interface confined within the mesoporous channels, and investigated the mechanism underlying their enhanced stability.

RESOURCE AVAILABILITY

Lead contact

Further information and requests for resources and reagents should be directed to and will be fulfilled by the lead contact, Dong Gu (DGu@scut.edu.cn).

Materials availability

This study did not generate new unique material.

Data and code availability

This study did not generate any datasets or code. All relevant data are available from the corresponding author (DGu@scut.edu.cn, DGu@whu.edu.cn) upon reasonable request.

ACKNOWLEDGMENTS

The work was supported by the National Key R&D Program of China (2023YFA1508001 and 2018YFE0201703), the "1000 Youth Talents Plan", the Particle Engineering Laboratory at Soochow University (SDHY2137), the Fundamental Research Funds for the Central Universities (2042019kf0230), and the China Postdoctoral Science Foundation (2024M752468). The authors would like to acknowledge the Center for Electron Microscopy at Wuhan University for their substantial support to TEM work. We acknowledge the beamtime at B18 of the Diamond Light Source (session number SP36367-1) for the XAFS measurements.

AUTHOR CONTRIBUTIONS

Y.Z., conceptualization, methodology, formal analysis, visualization, and formal analysis; Y.P. and W.X., review and editing; S.Z., XPS characterization; H.G. and F.R.W., XAFS characterization; H.Y., DFT calculations; D.G., review and editing, supervision, and funding acquisition.

DECLARATION OF INTERESTS

The authors declare no competing financial interest.

STAR★METHODS

Detailed methods are provided in the online version of this paper and include the following:

- KEY RESOURCES TABLE
- METHOD DETAILS
  - Catalyst synthesis
  - Characterization
  - Catalytic performance
  - Computational details
- QUANTIFICATION AND STATISTICAL ANALYSIS

SUPPLEMENTAL INFORMATION

Supplemental information can be found online at https://doi.org/10.1016/j.isci.2025.112582.

Received: March 3, 2025
Revised: April 4, 2025
Accepted: April 29, 2025
Published: May 3, 2025

REFERENCES

1. Akri, M., Zhao, S., Li, X., Zang, K., Lee, A.F., Isaacs, M.A., Xi, W., Gangarajula, Y., Luo, J., Ren, Y., et al. (2019). Atomically dispersed nickel as coke-resistant active sites for methane dry reforming. Nat. Commun. *10*, 5181. https://doi.org/10.1038/s41467-019-12843-w.
2. Tian, S., Yan, F., Zhang, Z., and Jiang, J. (2019). Calcium-looping reforming of methane realizes in situ CO_2 utilization with improved energy efficiency. Sci. Adv. *5*, eaav5077. https://doi.org/10.1126/sciadv.aav5077.
3. Buelens, L.C., Galvita, V.V., Poelman, H., Detavernier, C., and Marin, G.B. (2016). Super-dry reforming of methane intensifies CO_2 utilization via Le Chatelier's principle. Science *354*, 449–452. https://doi.org/10.1126/science.aah7161.
4. Gao, P., Li, S., Bu, X., Dang, S., Liu, Z., Wang, H., Zhong, L., Qiu, M., Yang, C., Cai, J., et al. (2017). Direct conversion of CO_2 into liquid fuels with high selectivity over a bifunctional catalyst. Nat. Chem. *9*, 1019–1024. https://doi.org/10.1038/nchem.2794.
5. Pakhare, D., and Spivey, J. (2014). A review of dry (CO_2) reforming of methane over noble metal catalysts. Chem. Soc. Rev. *43*, 7813–7837. https://doi.org/10.1039/C3CS60395D.
6. Qi, G., Davies, T.E., Nasrallah, A., Sainna, M.A., Howe, A.G.R., Lewis, R.J., Quesne, M., Catlow, C.R.A., Willock, D.J., He, Q., et al. (2022). Au-ZSM-5 catalyses the selective oxidation of CH_4 to CH_3OH and CH_3COOH using O_2. Nat. Catal. *5*, 45–54. https://doi.org/10.1038/s41929-021-00725-8.
7. Zhou, L., Martirez, J.M.P., Finzel, J., Zhang, C., Swearer, D.F., Tian, S., Robatjazi, H., Lou, M., Dong, L., Henderson, L., et al. (2020). Light-driven methane dry reforming with single atomic site antenna-reactor plasmonic photocatalysts. Nat. Energy *5*, 61–70. https://doi.org/10.1038/s41560-019-0517-9.
8. Song, Y., Ozdemir, E., Ramesh, S., Adishev, A., Subramanian, S., Harale, A., Albuali, M., Fadhel, B.A., Jamal, A., Moon, D., et al. (2020). Dry reforming of methane by stable Ni-Mo nanocatalysts on single-crystalline MgO. Science *367*, 777–781. https://doi.org/10.1126/science.aav2412.
9. Bradford, M.C.J., and Vannice, M.A. (1999). CO_2 Reforming of CH_4. Catal. Rev. *41*, 1–42. https://doi.org/10.1081/CR-100101948.
10. Wang, H., Cui, G., Lu, H., Li, Z., Wang, L., Meng, H., Li, J., Yan, H., Yang, Y., and Wei, M. (2024). Facilitating the dry reforming of methane with interfacial synergistic catalysis in an Ir@CeO_{2-x} catalyst. Nat. Commun. *15*, 3765. https://doi.org/10.1038/s41467-024-48122-6.
11. Abdulrasheed, A., Jalil, A.A., Gambo, Y., Ibrahim, M., Hambali, H.U., and Shahul Hamid, M.Y. (2019). A review on catalyst development for dry reforming of methane to syngas: Recent advances. Renew. Sustain. Energy Rev. *108*, 175–193. https://doi.org/10.1016/j.rser.2019.03.054.
12. Al-Fatesh, A.S., Patel, N., Fakeeha, A.H., Alotibi, M.F., Alreshaidan, S.B., and Kumar, R. (2024). Reforming of methane: Effects of active metals, supports, and promoters. Catal. Rev. *66*, 2209–2307. https://doi.org/10.1080/01614940.2023.2211447.
13. Joo, S., Kim, K., Kwon, O., Oh, J., Kim, H.J., Zhang, L., Zhou, J., Wang, J.-Q., Jeong, H.Y., Han, J.W., and Kim, G. (2021). Enhancing Thermocatalytic Activities by Upshifting the d-Band Center of Exsolved Co-Ni-Fe Ternary Alloy Nanoparticles for the Dry Reforming of Methane. Angew. Chem. Int. Ed. Engl. *60*, 15912–15919. https://doi.org/10.1002/anie.202101335.
14. Sandoval-Diaz, L., Cruz, D., Vuijk, M., Ducci, G., Hävecker, M., Jiang, W., Plodinec, M., Hammud, A., Ivanov, D., Götsch, T., et al. (2024). Metastable nickel-oxygen species modulate rate oscillations during dry reforming of methane. Nat. Catal. *7*, 161–171. https://doi.org/10.1038/s41929-023-01090-4.
15. Liu, Z., Lustemberg, P., Gutiérrez, R.A., Carey, J.J., Palomino, R.M., Vorokhta, M., Grinter, D.C., Ramírez, P.J., Matolín, V., Nolan, M., et al. (2017). In Situ Investigation of Methane Dry Reforming on Metal/Ceria(111) Surfaces: Metal-Support Interactions and C-H Bond Activation at Low Temperature. Angew. Chem. Int. Ed. *56*, 13041–13046. https://doi.org/10.1002/anie.201707538.
16. Liu, Z., Grinter, D.C., Lustemberg, P.G., Nguyen-Phan, T.-D., Zhou, Y., Luo, S., Waluyo, I., Crumlin, E.J., Stacchiola, D.J., Zhou, J., et al. (2016). Dry Reforming of Methane on a Highly-Active Ni-CeO_2 Catalyst: Effects of Metal-Support Interactions on C-H Bond Breaking. Angew. Chem. Int. Ed. Engl. *55*, 7455–7459. https://doi.org/10.1002/anie.201602489.
17. Kim, S.M., Abdala, P.M., Margossian, T., Hosseini, D., Foppa, L., Armutlulu, A., van Beek, W., Comas-Vives, A., Copéret, C., and Müller, C. (2017). Cooperativity and Dynamics Increase the Performance of NiFe Dry Reforming Catalysts. J. Am. Chem. Soc. *139*, 1937–1949. https://doi.org/10.1021/jacs.6b11487.
18. Zhang, H., Sun, P., Fei, X., Wu, X., Huang, Z., Zhong, W., Gong, Q., Zheng, Y., Zhang, Q., Xie, S., et al. (2024). Unusual facet and co-catalyst effects in TiO_2-based photocatalytic coupling of methane. Nat. Commun. *15*, 4453. https://doi.org/10.1038/s41467-024-48866-1.
19. Chen, G., Zhao, Y., Fu, G., Duchesne, P.N., Gu, L., Zheng, Y., Weng, X., Chen, M., Zhang, P., Pao, C.-W., et al. (2014). Interfacial Effects in Iron-Nickel Hydroxide-Platinum Nanoparticles Enhance Catalytic Oxidation. Science *344*, 495–499. https://doi.org/10.1126/science.1252553.
20. Graciani, J., Mudiyanselage, K., Xu, F., Baber, A.E., Evans, J., Senanayake, S.D., Stacchiola, D.J., Liu, P., Hrbek, J., Fernández Sanz, J., and Rodriguez, J.A. (2014). Highly active copper-ceria and copper-ceria-titania catalysts for methanol synthesis from CO_2. Science *345*, 546–550. https://doi.org/10.1126/science.1253057.
21. Yuan, W., Zhu, B., Fang, K., Li, X.-Y., Hansen, T.W., Ou, Y., Yang, H., Wagner, J.B., Gao, Y., Wang, Y., and Zhang, Z. (2021). In situ manipulation of the active Au-TiO_2 interface with atomic precision during CO oxidation. Science *371*, 517–521. https://doi.org/10.1126/science.abe3558.
22. Peng, H., Zhang, X., Han, X., You, X., Lin, S., Chen, H., Liu, W., Wang, X., Zhang, N., Wang, Z., et al. (2019). Catalysts in Coronas: A Surface Spatial Confinement Strategy for High-Performance Catalysts in Methane Dry Reforming. ACS Catal. *9*, 9072–9080. https://doi.org/10.1021/acscatal.9b00968.
23. Barroso-Quiroga, M.M., and Castro-Luna, A.E. (2010). Catalytic activity and effect of modifiers on Ni-based catalysts for the dry reforming of methane. Int. J. Hydrogen Energy *35*, 6052–6056. https://doi.org/10.1016/j.ijhydene.2009.12.073.
24. Khatri, J., Fakeeha, A.H., Kasim, S.O., Lanre, M.S., Abasaeed, A.E., Ibrahim, A.A., Kumar, R., and Al-Fatesh, A.S. (2021). Ceria promoted phosphate-zirconia supported Ni catalyst for hydrogen rich syngas production through dry reforming of methane. Int. J. Energy Res. *45*, 19289–19302. https://doi.org/10.1002/er.7026.
25. Fakeeha, A.H., Acharya, K., Ibrahim, A.A., Almutairi, G., Abu-Dahrieh, J.K., Abasaeed, A.E., Kumar, R., and Al-Fatesh, A.S. (2023). Role of promoters over yttria-zirconia supported Ni catalyst for dry reforming of methane. Energy Sci. Eng. *11*, 4366–4380. https://doi.org/10.1002/ese3.1586.
26. Khatri, J., Al-Fatesh, A.S., Fakeeha, A.H., Ibrahim, A.A., Abasaeed, A.E., Kasim, S.O., Osman, A.I., Patel, R., and Kumar, R. (2021). Ce promoted lanthana-zirconia supported Ni catalyst system: A ternary redox system for hydrogen production. Mol. Catal. *504*, 111498. https://doi.org/10.1016/j.mcat.2021.111498.
27. Al-Fatesh, A.S., Arafat, Y., Ibrahim, A.A., Atia, H., Fakeeha, A.H., Armbruster, U., Abasaeed, A.E., and Frusteri, F. (2018). Evaluation of Co-Ni/Sc-SBA–15 as a novel coke resistant catalyst for syngas production via CO_2 reforming of methane. Appl. Catal. Gen. *567*, 102–111. https://doi.org/10.1016/j.apcata.2018.09.012.
28. Peng, Y., Song, S., Liu, F., Yin, Z., Zhong, Y., Yi, X., Zheng, A., Schüth, F., and Gu, D. (2022). General Surface-Casting Synthesis of Mesoporous Metal Oxides with Hollow Structures and Ultrahigh Surface Areas. Chem. Mater. *34*, 7042–7057. https://doi.org/10.1021/acs.chemmater.2c01493.

29. Gu, D., Schmidt, W., Pichler, C.M., Bongard, H.-J., Spliethoff, B., Asahina, S., Cao, Z., Terasaki, O., and Schüth, F. (2017). Surface-Casting Synthesis of Mesoporous Zirconia with a CMK-5-Like Structure and High Surface Area. Angew. Chem. Int. Ed. Engl. *56*, 11222–11225. https://doi.org/10.1002/anie.201705042.

30. Zhang, Y., Zhao, Y., Otroshchenko, T., Lund, H., Pohl, M.-M., Rodemerck, U., Linke, D., Jiao, H., Jiang, G., and Kondratenko, E.V. (2018). Control of coordinatively unsaturated Zr sites in ZrO_2 for efficient C–H bond activation. Nat. Commun. *9*, 3794. https://doi.org/10.1038/s41467-018-06174-5.

31. Yang, Y., Sun, X., Han, G., Liu, X., Zhang, X., Sun, Y., Zhang, M., Cao, Z., and Sun, Y. (2019). Enhanced Electrocatalytic Hydrogen Oxidation on Ni/NiO/C Derived from a Nickel-Based Metal–Organic Framework. Angew. Chem. Int. Ed. Engl. *58*, 10644–10649. https://doi.org/10.1002/anie.201905430.

32. Zhao, D., Feng, J., Huo, Q., Melosh, N., Fredrickson, G.H., Chmelka, B.F., and Stucky, G.D. (1998). Triblock Copolymer Syntheses of Mesoporous Silica with Periodic 50 to 300 Angstrom Pores. Science *279*, 548–552. https://doi.org/10.1126/science.279.5350.548.

33. Gu, D., Jia, C.-J., Weidenthaler, C., Bongard, H.-J., Spliethoff, B., Schmidt, W., and Schüth, F. (2015). Highly Ordered Mesoporous Cobalt-Containing Oxides: Structure, Catalytic Properties, and Active Sites in Oxidation of Carbon Monoxide. J. Am. Chem. Soc. *137*, 11407–11418. https://doi.org/10.1021/jacs.5b06336.

34. Dong, J., Fu, Q., Li, H., Xiao, J., Yang, B., Zhang, B., Bai, Y., Song, T., Zhang, R., Gao, L., et al. (2020). Reaction-Induced Strong Metal-Support Interactions between Metals and Inert Boron Nitride Nanosheets. J. Am. Chem. Soc. *142*, 17167–17174. https://doi.org/10.1021/jacs.0c08139.

35. Cheng, Q., Yao, X., Ou, L., Hu, Z., Zheng, L., Li, G., Morlanes, N., Cerrillo, J.L., Castaño, P., Li, X., et al. (2023). Highly Efficient and Stable Methane Dry Reforming Enabled by a Single-Site Cationic Ni Catalyst. J. Am. Chem. Soc. *145*, 25109–25119. https://doi.org/10.1021/jacs.3c04581.

36. Arrigo, R., Gallarati, S., Schuster, M.E., Seymour, J.M., Gianolio, D., da Silva, I., Callison, J., Feng, H., Proctor, J.E., Ferrer, P., et al. (2020). Influence of Synthesis Conditions on the Structure of Nickel Nanoparticles and their Reactivity in Selective Asymmetric Hydrogenation. ChemCatChem *12*, 1491–1503. https://doi.org/10.1002/cctc.201901955.

37. Yao, Y., Li, B., Gao, X., Yang, Y., Yu, J., Lei, J., Li, Q., Meng, X., Chen, L., and Xu, D. (2023). Highly Efficient Solar-Driven Dry Reforming of Methane on a Rh/$LaNiO_3$ Catalyst through a Light-induced Metal-To-Metal Charge Transfer Process. Adv. Mater. *35*, 2303654. https://doi.org/10.1002/adma.202303654.

38. Rao, Z., Cao, Y., Huang, Z., Yin, Z., Wan, W., Ma, M., Wu, Y., Wang, J., Yang, G., Cui, Y., et al. (2021). Insights into the Nonthermal Effects of Light in Dry Reforming of Methane to Enhance the H_2/CO Ratio Near Unity over Ni/Ga_2O_3. ACS Catal. *11*, 4730–4738. https://doi.org/10.1021/acscatal.0c04826.

39. Zheng, X., Han, X., Cao, Y., Zhang, Y., Nordlund, D., Wang, J., Chou, S., Liu, H., Li, L., Zhong, C., et al. (2020). Identifying Dense $NiSe_2$/$CoSe_2$ Heterointerfaces Coupled with Surface High-Valence Bimetallic Sites for Synergistically Enhanced Oxygen Electrocatalysis. Adv. Mater. *32*, 2000607. https://doi.org/10.1002/adma.202000607.

40. He, D., Zhang, Y., Li, T., Chen, D., Wang, H., Zhang, L., Liu, J., Cao, X., Lu, J., and Luo, Y. (2025). Designing Ultra-Stable and Surface-Exposed Ni Nanoparticles with Dually Confined Microenvironment for High-Temperature Methane Dry Reforming. Adv. Funct. Mater. *35*, 2412895. https://doi.org/10.1002/adfm.202412895.

41. Zhang, X., Pei, C., Chang, X., Chen, S., Liu, R., Zhao, Z.-J., Mu, R., and Gong, J. (2020). FeO_6 Octahedral Distortion Activates Lattice Oxygen in Perovskite Ferrite for Methane Partial Oxidation Coupled with CO_2 Splitting. J. Am. Chem. Soc. *142*, 11540–11549. https://doi.org/10.1021/jacs.0c04643.

42. Pu, Z., Liu, Q., Chen, C., and Wang, F. (2024). Promoting surface lattice oxygen and oxygen vacancy of CeO_2 for photothermal methane dry reforming over Ni/CeO_2 catalysts. Chem. Eng. J. *497*, 154861. https://doi.org/10.1016/j.cej.2024.154861.

43. Gao, X.Y., Ashok, J., Widjaja, S., Hidajat, K., and Kawi, S. (2015). Ni/SiO_2 catalyst prepared via Ni-aliphatic amine complexation for dry reforming of methane: Effect of carbon chain number and amine concentration. Appl. Catal. Gen. *503*, 34–42. https://doi.org/10.1016/j.apcata.2015.07.005.

44. Basahel, S.N., Ali, T.T., Mokhtar, M., and Narasimharao, K. (2015). Influence of crystal structure of nanosized ZrO_2 on photocatalytic degradation of methyl orange. Nanoscale Res. Lett. *10*, 73. https://doi.org/10.1186/s11671-015-0780-z.

45. Yang, C., Pei, C., Luo, R., Liu, S., Wang, Y., Wang, Z., Zhao, Z.-J., and Gong, J. (2020). Strong Electronic Oxide–Support Interaction over In_2O_3/ZrO2 for Highly Selective CO_2 Hydrogenation to Methanol. J. Am. Chem. Soc. *142*, 19523–19531. https://doi.org/10.1021/jacs.0c07195.

46. Li, W., Nie, X., Jiang, X., Zhang, A., Ding, F., Liu, M., Liu, Z., Guo, X., and Song, C. (2018). ZrO2 support imparts superior activity and stability of Co catalysts for CO_2 methanation. Appl. Catal. B Environ. *220*, 397–408. https://doi.org/10.1016/j.apcatb.2017.08.048.

47. Wu, C., Lin, L., Liu, J., Zhang, J., Zhang, F., Zhou, T., Rui, N., Yao, S., Deng, Y., Yang, F., et al. (2020). Inverse ZrO_2/Cu as a highly efficient methanol synthesis catalyst from CO_2 hydrogenation. Nat. Commun. *11*, 5767. https://doi.org/10.1038/s41467-020-19634-8.

48. Tian, J., Shao, Q., Zhao, J., Pan, D., Dong, M., Jia, C., Ding, T., Wu, T., and Guo, Z. (2019). Microwave solvothermal carboxymethyl chitosan templated synthesis of TiO_2/ZrO_2 composites toward enhanced photocatalytic degradation of Rhodamine B. J. Colloid Interface Sci. *541*, 18–29. https://doi.org/10.1016/j.jcis.2019.01.069.

49. Liu, Z., Gao, Z., and Wu, Q. (2021). Activation of persulfate by magnetic zirconium-doped manganese ferrite for efficient degradation of tetracycline. Chem. Eng. J. *423*, 130283. https://doi.org/10.1016/j.cej.2021.130283.

50. Bi, F., Ma, S., Gao, B., Liu, B., Huang, Y., Qiao, R., and Zhang, X. (2024). Boosting toluene deep oxidation by tuning metal-support interaction in MOF-derived Pd@ZrO_2 catalysts: The role of interfacial interaction between Pd and ZrO_2. Fuel *357*, 129833. https://doi.org/10.1016/j.fuel.2023.129833.

51. Park, K.S., Goag, T.Y., Kwon, J.H., Park, Y.M., Yu, J.S., Jeong, H.E., Choung, J.W., and Bae, J.W. (2021). Effects of spatially confined nickel nanoparticles in surface-pretreated hydrophobic SBA-15 for dry reforming of CH_4 with CO_2. J. CO2 Util. *51*, 101629. https://doi.org/10.1016/j.jcou.2021.101629.

52. Kim, S., Lauterbach, J., and Sasmaz, E. (2021). Yolk-Shell Pt-NiCe@SiO_2 Single-Atom-Alloy Catalysts for Low-Temperature Dry Reforming of Methane. ACS Catal. *11*, 8247–8260. https://doi.org/10.1021/acscatal.1c01223.

53. Du, Y., Qin, C., Xu, Y., Xu, D., Bai, J., Ma, G., and Ding, M. (2021). Ni nanoparticles dispersed on oxygen vacancies-rich CeO_2 nanoplates for enhanced low-temperature CO_2 methanation performance. Chem. Eng. J. *418*, 129402. https://doi.org/10.1016/j.cej.2021.129402.

54. Song, Q., Ran, R., Wu, X., Si, Z., and Weng, D. (2023). Dry reforming of methane over Ni catalysts supported on micro- and mesoporous silica. J. CO2 Util. *68*, 102387. https://doi.org/10.1016/j.jcou.2022.102387.

55. Kim, K.Y., Lee, J.H., Lee, H., Noh, W.Y., Kim, E.H., Ra, E.C., Kim, S.K., An, K., and Lee, J.S. (2021). Layered Double Hydroxide-Derived Intermetallic $Ni_3GaC_{0.25}$ Catalysts for Dry Reforming of Methane. ACS Catal. *11*, 11091–11102. https://doi.org/10.1021/acscatal.1c02200.

56. Li, H., Hao, C., Tian, J., Wang, S., and Zhao, C. (2022). Ultra-durable Ni-Ir/$MgAl_2O_4$ catalysts for dry reforming of methane enabled by dynamic balance between carbon deposition and elimination. Chem Catal. *2*, 1748–1763. https://doi.org/10.1016/j.checat.2022.05.005.

57. Guo, D., Lu, Y., Ruan, Y., Zhao, Y., Zhao, Y., Wang, S., and Ma, X. (2020). Effects of extrinsic defects originating from the interfacial reaction of

CeO_{2-x}-nickel silicate on catalytic performance in methane dry reforming. Appl. Catal. B Environ. *277*, 119278. https://doi.org/10.1016/j.apcatb.2020.119278.

58. Bu, K., Kuboon, S., Deng, J., Li, H., Yan, T., Chen, G., Shi, L., and Zhang, D. (2019). Methane dry reforming over boron nitride interface-confined and LDHs-derived Ni catalysts. Appl. Catal. B Environ. *252*, 86–97. https://doi.org/10.1016/j.apcatb.2019.04.007.
59. Marinho, A.L.A., Rabelo-Neto, R.C., Epron, F., Bion, N., Toniolo, F.S., and Noronha, F.B. (2020). Embedded Ni nanoparticles in $CeZrO_2$ as stable catalyst for dry reforming of methane. Appl. Catal. B Environ. *268*, 118387. https://doi.org/10.1016/j.apcatb.2019.118387.
60. Li, Y., Liu, X., Wu, T., Zhang, X., Han, H., Liu, X., Chen, Y., Tang, Z., Liu, Z., Zhang, Y., et al. (2024). Pulsed laser induced plasma and thermal effects on molybdenum carbide for dry reforming of methane. Nat. Commun. *15*, 5495. https://doi.org/10.1038/s41467-024-49771-3.
61. Yu, J., Le, T., Jing, D., Stavitski, E., Hunter, N., Lalit, K., Leshchev, D., Resasco, D.E., Sargent, E.H., Wang, B., and Huang, W. (2023). Balancing elementary steps enables coke-free dry reforming of methane. Nat. Commun. *14*, 7514. https://doi.org/10.1038/s41467-023-43277-0.
62. Colombo, R., Moroni, G., Negri, C., Delen, G., Monai, M., Donazzi, A., Weckhuysen, B.M., and Maestri, M. (2024). Surface Carbon Formation and its Impact on Methane Dry Reforming Kinetics on Rhodium-Based Catalysts by Operando Raman Spectroscopy. Angew. Chem. Int. Ed. Engl. *63*, e202408668. https://doi.org/10.1002/anie.202408668.
63. Weber, S., Batey, D., Cipiccia, S., Stehle, M., Abel, K.L., Gläser, R., and Sheppard, T.L. (2021). Hard X-Ray Nanotomography for 3D Analysis of Coking in Nickel-Based Catalysts. Angew. Chem. Int. Ed. Engl. *60*, 21772–21777. https://doi.org/10.1002/anie.202106380.
64. Wang, D., Littlewood, P., Marks, T.J., Stair, P.C., and Weitz, E. (2022). Coking Can Enhance Product Yields in the Dry Reforming of Methane. ACS Catal. *12*, 8352–8362. https://doi.org/10.1021/acscatal.2c02045.
65. Xiong, H., Dong, Y., Hu, C., Chen, Y., Liu, H., Long, R., Kong, T., and Xiong, Y. (2024). Highly Efficient and Selective Light-Driven Dry Reforming of Methane by a Carbon Exchange Mechanism. J. Am. Chem. Soc. *146*, 9465–9475. https://doi.org/10.1021/jacs.4c02427.
66. Lu, Y., Kang, L., Guo, D., Zhao, Y., Zhao, Y., Wang, S., and Ma, X. (2021). Double-Site Doping of a V Promoter on Ni_x-V-MgAl Catalysts for the DRM Reaction: Simultaneous Effect on CH_4 and CO_2 Activation. ACS Catal. *11*, 8749–8765. https://doi.org/10.1021/acscatal.1c01299.
67. Bai, S., Liu, F., Huang, B., Li, F., Lin, H., Wu, T., Sun, M., Wu, J., Shao, Q., Xu, Y., and Huang, X. (2020). High-efficiency direct methane conversion to oxygenates on a cerium dioxide nanowires supported rhodium single-atom catalyst. Nat. Commun. *11*, 954. https://doi.org/10.1038/s41467-020-14742-x.
68. Ozkan, D.M., Uzun, A., Caglayan, B.S., and Aksoylu, A.E. (2023). A DFT study on the role of oxygen vacancy on m-ZrO_2 (111) in adsorption and dissociation of CO_2. Surf. Sci. *736*, 122336. https://doi.org/10.1016/j.susc.2023.122336.
69. Shi, X.-R., Wang, P., Jing, C., Wu, K., Xu, S., and Klötzer, B. (2023). The formation of O vacancy on ZrO_2/Pd and its effect on methane dry reforming: Insights from DFT and microkinetic modeling. Appl. Surf. Sci. *619*, 156679. https://doi.org/10.1016/j.apsusc.2023.156679.
70. Sun, J., Yamaguchi, D., Tang, L., Periasamy, S., Ma, H., Hart, J.N., and Chiang, K. (2022). Enhancement of oxygen exchanging capability by loading a small amount of ruthenium over ceria-zirconia on dry reforming of methane. Adv. Powder Technol. *33*, 103407. https://doi.org/10.1016/j.apt.2021.103407.
71. Watanabe, H., Muto, S., and Ogura, T. (2024). Impact of dopant X in zirconia on carbon deposition at the Nickel/X-stabilized zirconia(XSZ) surface in dry CH_4 and CH_4/H_2O environments: First-principles density functional theory calculation and experimental study. Int. J. Hydrogen Energy *50*, 1155–1166. https://doi.org/10.1016/j.ijhydene.2023.10.075.
72. Zhang, C., Niu, J., Guo, B., Liu, H., Jin, Y., and Ran, J. (2024). Effect of Cu doping on Ni surface on CO formation pathways during the methane dry reforming reaction. Mol. Catal. *560*, 114125. https://doi.org/10.1016/j.mcat.2024.114125.
73. Jiao, H., and Wang, G.-C. (2025). A Comprehensive Theoretical Study of the Mechanism for Dry Reforming of Methane on a Ni_4/ZrO_2(101) Catalyst Under External Electric Fields: The Role of Interface and Oxygen Vacancy. ACS Catal. *15*, 3846–3859. https://doi.org/10.1021/acscatal.4c05758.
74. Zhao, D., Feng, J., Huo, Q., Melosh, N., Fredrickson, G.H., Chmelka, B.F., and Stucky, G.D. (1998). Triblock copolymer syntheses of mesoporous silica with periodic 50 to 300 angstrom pores. Science *279*, 548–552. https://doi.org/10.1126/science.279.5350.548.
75. Ravel, B., and Newville, M. (2005). Data analysis for X-ray absorption spectroscopy using. J. Synchrotron Radiat. *12*, 537–541. https://doi.org/10.1107/S0909049505012719.
76. Zabinsky, S.I., Rehr, J.J., Ankudinov, A., Albers, R.C., and Eller, M.J. (1995). Multiple-Scattering Calculations of X-Ray-Absorption Spectra. Phys. Rev. B *52*, 2995–3009. https://doi.org/10.1103/PhysRevB.52.2995.
77. Kresse, G., and Furthmüller, J. (1996). Efficiency of ab-initio total energy calculations for metals and semiconductors using a plane-wave basis set. Comput. Mater. Sci. *6*, 15–50. https://doi.org/10.1016/0927-0256(96)00008-0.
78. Blöchl, P.E. (1994). Projector augmented-wave method. Phys. Rev. B *50*, 17953–17979. https://doi.org/10.1103/PhysRevB.50.17953.
79. Perdew, J.P., Burke, K., and Ernzerhof, M. (1996). Generalized Gradient Approximation Made Simple. Phys. Rev. Lett. *77*, 3865–3868. https://doi.org/10.1103/PhysRevLett.77.3865.
80. Henkelman, G., Uberuaga, B.P., and Jónsson, H. (2000). A climbing image nudged elastic band method for finding saddle points and minimum energy paths. J. Chem. Phys. *113*, 9901–9904. https://doi.org/10.1063/1.1329672.

STAR★METHODS

KEY RESOURCES TABLE

REAGENT or RESOURCE	SOURCE	IDENTIFIER
Chemicals, peptides, and recombinant proteins		
Triblock copolymer poly(ethylene oxide)-*b*-poly(propylene oxide)-*b*-poly-(ethylene oxide) PEO-PPO-PEO, Pluronic P123, average Mn ~5800	Merck & Co. Inc	CAS: 9003-11-6
Tetraethoxysilane TEOS	China National Medicines Co. Ltd	CAS: 78-10-4
Nickel(II) nitrate hexahydrate $Ni(NO_3)_2{\cdot}6H_2O$	China National Medicines Co. Ltd	CAS: 13478-00-7
Zirconium Oxychloride Octahydrate $ZrOCl_2{\cdot}8H_2O$	China National Medicines Co. Ltd	CAS: 13520-92-8
Software and algorithms		
Origin	OriginLab Co. Ltd	https://www.originlab.com/
Microsoft office	Microsoft	https://www.microsoft.com/zh-cn/
VASP	Tri-I·Biotech(Shanghai),·Ltd.	https://www.vasp.at/
Jade	Materials Data, Inc.	https://jade.tilab.com/download/jade/license/jade-download/

METHOD DETAILS

Catalyst synthesis

Synthesis of SBA-15-OH

Mesoporous silica SBA-15-OH was synthesized following our previously reported method.[28,74] In a typical procedure, 20.0 g of triblock copolymer poly(ethylene oxide)-*b*-poly(propylene oxide)-*b*-poly-(ethylene oxide) (PEO−PPO−PEO, Pluronic P123, average Mn ~5800) was dissolved in 650 mL of distilled water and 100 mL of concentrated HCl. The solution was stirred at 38°C for 2 h until Pluronic P123 was completely dissolved. Subsequently, 41.6 g of tetraethoxysilane (TEOS) was slowly added under identical conditions and allowed to react for 24 h. The resulting suspension was transferred to a hydrothermal reactor and treated at 110°C for 24 h. After filtration, the obtained surfactant-silica composite was thoroughly dried at 50°C. Finally, the SBA-15-OH support was obtained by treating the composite with a mixture of concentrated nitric acid and hydrogen peroxide at 80°C for 3 h, followed by filtration, washing, and drying.

Preparation of ZrSBA-15-OH

The ZrO_2 surface-coated mesoporous silica support (denoted as ZrSBA-15-OH) was prepared following a previously reported method.[28] In a typical procedure, 1.12 g of zirconium oxychloride octahydrate ($ZrOCl_2{\cdot}8H_2O$) was dissolved in 12 mL of deionized water (H_2O) to form a homogeneous solution. Then, 1.0 g of SBA-15-OH was added to the solution and stirred at room temperature for 2 h. The mixture was then evaporated in an oven at 90°C and dried for 2 h. Finally, the ZrSBA-15-OH support was obtained by calcination at 300°C for 4 h in a muffle furnace.

Preparation of SCO-Zr

The pure mesoporous ZrO_2 support was obtained by treating the ZrSBA-15-OH sample in 2 M NaOH at 70°C to remove silica template.

Synthesis of Ni-based catalysts

All Ni-based catalysts were synthesized via an impregnation-calcination method. Specifically, 0.26 g of nickel nitrate hexahydrate ($Ni(NO_3)_2{\cdot}6H_2O$) was dissolved in 12 mL of deionized water. Once the metal nitrate was fully dissolved, 1.0 g of different supports (SBA-15-OH, ZrSBA-15-OH, SCO-Zr, or commercial ZrO_2) was added to the solution and stirred thoroughly for 2 h. The solvent was then removed by evaporation in an oven at 70°C for approximately 2 h. Finally, the Ni-based catalysts were obtained by pyrolysis in a muffle furnace at 500°C for 2 h. The resulting catalysts were denoted as Ni/SBA-15-OH, Ni/ZrSBA-15-OH, Ni/SCO-Zr, and Ni/commercial ZrO_2, corresponding to the respective supports used.

Characterization

The phase composition and crystal structure of the samples were analyzed using an X-ray diffractometer (XRD) (Rigaku SmartLab SE, 2.2 kW, Japan) with Cu Kα radiation (λ = 0.154 nm) at a tube current of 50 mA and a voltage of 40 kV, covering the 2θ range

of 10–80°. The specific surface area, pore volume, and pore size distribution were determined using a TriStar II 3020 analyzer (Micromeritics, USA) at 77 K. Before adsorption measurements, each sample was degassed under vacuum at 150°C for at least 6 h to remove physically adsorbed species. Transmission electron microscopy (TEM), high-resolution TEM (HR-TEM) imaging, scanning transmission electron microscopy (STEM) and energy-dispersive X-ray spectroscopy (EDX) mapping were conducted using a JEM-F200 multipurpose electron microscope (JEOL Ltd., Japan) and a JEM-NEOARM microscope with a Schottky cold field emission gun at School of Physics and Technology, Wuhan University.

The actual nickel content was determined by inductively coupled plasma optical emission spectrometry (ICP-OES) using an Agilent ICP-OES 730 instrument (Agilent, USA). The coke content of catalysts after stability tests was measured using a METTLER TOLEDO TGA/DSC3+ thermogravimetric analyzer (METTLER TOLEDO, Switzerland). Raman spectra were acquired with a LabRAM HR Evolution Raman spectrometer (Horiba, France) using a 532 nm Ar-ion laser to analyze carbon species after stability testing. X-ray photoelectron spectroscopy (XPS) was performed using a Thermo Fisher Scientific ESCALAB 250Xi spectrometer (Thermo Fisher Scientific, USA) with a monochromatic Al Kα source (1486.6 eV) at Institute of Materials Science and Devices, Suzhou University of Science and Technology. Binding energies were calibrated using the C 1s signal at 284.8 eV as a reference.

X-ray absorption near-edge structure (XANES) and extended X-ray absorption fine structure (EXAFS) of the Ni K-edge were conducted at the Diamond Light Source (UK) and Spring-8 (Japan). Data reduction, analysis, and EXAFS fitting were performed using the Athena and Artemis programs within the Demeter data analysis package, which utilizes the FEFF6 program for EXAFS data fitting.[75,76] The energy calibration of the sample was conducted using a Ni foil standard, which was measured simultaneously as a reference. A linear function was subtracted from the pre-edge region, and the edge jump was normalized using Athena software. The $\chi(k)$ data were obtained by subtracting a smooth third-order polynomial that approximates the absorption background of an isolated atom. The k^3-weighted $\chi(k)$ data were Fourier transformed after applying a Hanning window function ($\Delta k = 1.0$). For EXAFS modeling, the global amplitude parameters (coordination number (CN), bond distance (R), Debye-Waller factor (σ^2), and energy shift (ΔE_0)) were obtained through nonlinear least-squares fitting of the EXAFS equation to the Fourier transformed data in R-space using Artemis software. The EXAFS of Ni foil was fitted first, and the obtained amplitude reduction factor ($S_0^2 = 0.782$) was used in the EXAFS analysis to determine the coordination numbers (CNs) of the sample.

CH_4 and CO_2 temperature-programmed surface reactions (TPSR) were conducted using a Bel Cata II apparatus integrated with an online mass spectrometer. A total of 100 mg of catalyst was pretreated at 500°C for 2 h under 5.0 vol % hydrogen in argon (Ar) (30 mL min^{-1}). After pretreatment, the catalyst was cooled to room temperature under Ar flow, and a mixture of 20 vol % CH_4 in Ar (30 mL min^{-1}) was introduced into the reactor. Once the mass spectrometry baseline stabilized, the reaction temperature was ramped up to 750 °C at a rate of 10 °C min^{-1} and maintained for 30 min, during which the corresponding mass signals for CH_4-TPSR were recorded. Subsequently, the CH_4/Ar gas mixture was switched to pure Ar, and the system was cooled to room temperature. Then, a mixture of CO_2 and Ar (30 mL min^{-1}) was introduced into the reactor. Once the mass spectrometry signal baseline stabilized, the CO_2-TPSR experiment was performed, and the characteristic mass signals were recorded accordingly.

Hydrogen temperature-programmed reduction (H_2-TPR) experiment was conducted using a iChem-700 instrument. Typically, 50 mg of catalyst was loaded into a U-shaped quartz tube reactor. Before measurement, the catalyst was pretreated under helium (He) flow (30 mL min^{-1}) at 150°C for 30 min. The sample was then cooled to ambient temperature under He flow. Subsequently, a 4.5 vol % H_2/N_2 gas mixture was introduced into the reactor, and the temperature-programmed reduction experiment was performed. The thermal conductivity detector (TCD) signal was recorded once the baseline stabilized.

Catalytic performance

The catalytic performance for the dry reforming of methane (DRM) was evaluated in a fixed-bed reactor under atmospheric pressure. Typically, 50 mg of catalyst was homogeneously mixed with 300 mg of quartz sand (250−500 μm) and loaded into a quartz reaction tube. Before measurement, the catalyst was reduced *in-situ* at 500°C for 2 h under a 4.5 vol % H_2/N_2 gas mixture (50 mL min^{-1}). After pretreatment, high-purity N_2 was introduced into the reactor to remove any residual gas mixtures. Subsequently, the reaction gas mixture (CH_4:CO_2:N_2 = 2:2:1, 50 mL min^{-1}, corresponding to a wight hourly space velocity (WHSV) of 30,000 mL g_{cat}^{-1} h^{-1}) was introduced once the temperature reached 550°C. After maintaining this temperature for 15 min, the gas composition was analyzed using gas chromatography (Thermo Scientific TRACE 1310, USA) with a thermal conductivity detector (TCD). Methane and carbon dioxide conversions were calculated using nitrogen as the internal standard, according to the following equations:

$$Conv._{(CH_4)} = \frac{\text{Moles of } (CH_4)\text{in} - \text{Moles of } (CH_4)\text{out}}{\text{Moles of } (CH_4)\text{in}} * 100\% \quad \text{(Equation 1)}$$

$$Conv._{(CO_2)} = \frac{\text{Moles of } (CO_2)\text{in} - \text{Moles of } (CO_2)\text{out}}{\text{Moles of } (CO_2)\text{in}} * 100\% \quad \text{(Equation 2)}$$

$Conv._{(CH4)}$ and $Conv._{(CO2)}$ corresponds to the conversion of methane and carbon dioxide, respectively.

Computational details

All density functional theory (DFT) calculations were performed using the Vienna ab-initio simulation package (VASP).[77] The projector-augmented wave method[78] was emploted with the generalized gradient approximation (GGA) of Perdew-Burke-Ernzerhof

(PBE).[79] An energy cut-off of 520 eV was used to guarantee the accuracy. The electronic convergence criterion was set to 10^{-5} eV. The Brillouin zone was sampled with a grid spacing of approximately 0.2 $Å^{-1}$ for bulk calculations, and only the Γ point was considered for all slab calculations. The $1 \times 1 \times 3$ orthogonal SiO_2(001) slab and ZrO_2(100) slab, each adsorped with one Ni atom on the surface, were constructed with a vacuum of 10 Å. Atomic layers below the top two layers were all fixed in geometric relaxations for the initial SiO_2-Ni and ZrO_2-Ni slabs. The energetically preferable Ni sites were determined by considering different initial Ni sites on the surface. The optimal SiO_2-Ni and ZrO_2-Ni slabs were then extended by 3×3 to consider different adsorbates. Then, the preferable sites for different adsorbates were determined by the atomic relaxation of different initial positions. More detailed structural information of the final constructed models are summarized in Table S6. The climbing-image nudged elastic band (CINEB) method[80] with three images was employed to estimate the corresponding reaction energy barriers.

QUANTIFICATION AND STATISTICAL ANALYSIS

The statistical analysis for average particle size (Figures 1D, S3D, S5B, S6C, and S16F) was performed using Origin (OriginLab).